Tectonics®

RESEARCH ARTICLE
10.1029/2024TC008752

Key Points:

- New LiDAR data allows identification of over 1,000 extensional faults across the Yellowstone caldera
- Kinematic analysis on these structures and modern GPS data indicate that these faults are part of one actively evolving extensional system
- Integration with previous studies suggests that the extensional system must also link to the Teton and East Gallatin fault systems

Supporting Information:

Supporting Information may be found in the online version of this article.

Correspondence to:

M. L. Swallom,
meredith.odell@uky.edu

Citation:

Swallom, M. L., Thigpen, J. R., Dortch, J. M., Johnson, S. E., Goldsby, R. C., Woolery, E. W., et al. (2026). Modern crustal extension across the Yellowstone caldera indicates linkage of the Teton and East Gallatin faults. *Tectonics*, *45*, e2024TC008752. https://doi.org/10.1029/2024TC008752

Received 9 DEC 2024
Accepted 24 FEB 2026

Author Contributions:

Conceptualization: Meredith L. Swallom, J. Ryan Thigpen, Ryan C. Goldsby, Rachel M. Hoar
Formal analysis: Meredith L. Swallom, J. Ryan Thigpen, Sarah E. Johnson
Funding acquisition: J. Ryan Thigpen, Edward W. Woolery, Michael M. McGlue, Kevin M. Yeager
Methodology: Meredith L. Swallom, J. Ryan Thigpen, Jason M. Dortch, Stephanie Vicroy
Resources: Summer J. Brown
Supervision: J. Ryan Thigpen
Validation: Jason M. Dortch, Edward W. Woolery
Writing – original draft: Meredith L. Swallom
Writing – review & editing: J. Ryan Thigpen, Jason M. Dortch, Sarah E. Johnson, Ryan C. Goldsby, Edward W. Woolery, Summer J. Brown, Michael M. McGlue, Kevin M. Yeager

Modern Crustal Extension Across the Yellowstone Caldera Indicates Linkage of the Teton and East Gallatin Faults

Meredith L. Swallom[1,2], J. Ryan Thigpen[1], Jason M. Dortch[2], Sarah E. Johnson[1], Ryan C. Goldsby[1], Edward W. Woolery[1], Summer J. Brown[1], Rachel M. Hoar[1], Stephanie Vicroy[1], Michael M. McGlue[1], and Kevin M. Yeager[3]

[1]Department of Earth and Environmental Sciences, University of Kentucky, Lexington, KY, USA, [2]Kentucky Geological Survey, University of Kentucky, Lexington, KY, USA, [3]Department of Ocean and Earth Sciences, Old Dominion University, Norfolk, VA, USA

Abstract The anomalously low-relief topography of the eastern Snake River Plain (ESRP) was produced by southwest Miocene migration of North America over the Yellowstone mantle plume. Multiple fault-related mountain ranges abruptly terminate at the plain margins, and it has been posited that migration over the plume drove east-west extension of the ESRP and adjacent Basin and Range, with the extensional footwall ranges that were continuous across the ESRP being "erased" by cooling-related crustal subsidence. However, direct evidence that these extensional systems were once continuous across the ESRP has remained limited, and questions remain regarding the process of "erasing" topography across the ESRP, particularly adjacent to the modern Yellowstone caldera. Analysis of recently acquired LiDAR data in the Yellowstone region reveals a dominant north-south trending extensional zone that spans the Yellowstone caldera and aligns with the active Teton and East Gallatin normal faults. Displacement analysis of these structures, when integrated with geophysical and geodetic data, indicates a kinematic linkage between the Teton and East Gallatin systems and provides critical evidence that these active faults were originally continuous across the hotspot track. Unlike other ranges that terminate against the ESRP, the removal of paleo-Teton and East Gallatin footwall topography cannot be explained by crustal subsidence due to cooling, given the elevated heat flow in the vicinity of Yellowstone. We propose that the collapse of these paleo-ranges into the calderas following the Huckleberry Ridge (~2.06 Ma) and Lava Creek (~0.6 Ma) eruptions can, at least in part, explain the removal of footwall topography.

Plain Language Summary The Teton Range, like many other Basin and Range mountains, loses relief rapidly at the margin of the topographically flat Snake River Plain. It has been proposed that the Teton fault system must continue north across the Yellowstone caldera to adhere to standard fault length-displacement relationships. Though a lack of any modern mountain topography has made this difficult to corroborate, new LiDAR data reveals over 1,000 active fault scarps spanning the zone between the Teton and East Gallatin faults. Displacement analysis indicates that these faults move at rates which allow them to logically link to these larger fault systems. In addition to these faults representing a likely structural connection between two mountain ranges, regional geophysical anomalies indicate that, at depth within the Yellowstone caldera, dense footwall blocks may be present. Therefore, though the hotspot could have "collapsed" topography associated with a longer Teton fault system, the extensional system itself persists. These findings may facilitate improved assessments of regional seismic hazard.

1. Introduction

In the northern Basin and Range in Idaho, the relatively low-relief eastern Snake River Plain (ESRP) marks, in part, the migration track of the Yellowstone hotspot (Pierce & Morgan, 2009). On the northern and southern margins of the ESRP, multiple high-relief (>1.5 km) mountain ranges represent the uplifted footwalls of northern Basin and Range normal faults (Figure 1a). This abrupt relief transition between the ESRP and the surrounding Basin and Range has been attributed to subsidence of the ESRP to produce >4.5 km of structural relief and crustal flexure at the margins following emplacement of a mid-crustal mafic sill (McQuarrie & Rodgers, 1998; Peng & Humphreys, 1998; Rodgers et al., 2002; Sparlin et al., 1982). Furthermore, studies examining the timing of Basin and Range extension and volcanism in the ESRP led to the "seismic parabola" model, wherein extension within the ESRP drives the observed Basin and Range extension, which becomes progressively younger moving east,

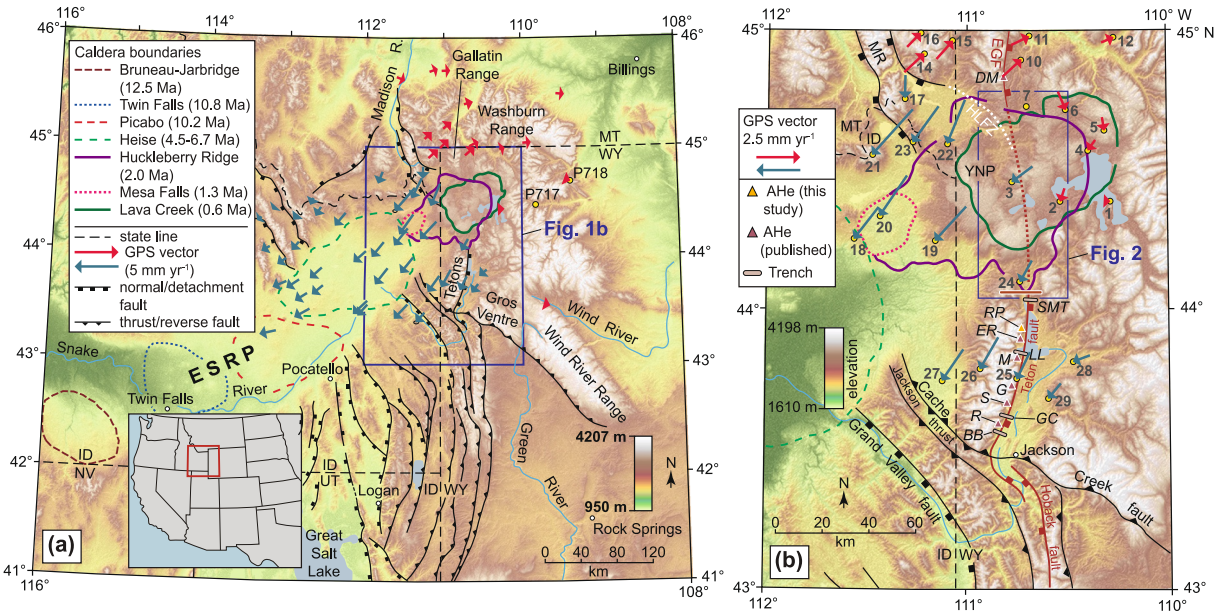

Figure 1. (a) Regional digital elevation model of the northern Basin and Range showing the eastern Snake River Plain (ESRP) marking the Yellowstone hotspot migration path and timing of major caldera forming eruptions (Pierce & Morgan, 2009). The abrupt topographic break along the margins of the ESRP highlights the relationship between caldera migration and topographic modification. GPS velocity vectors derived from the UNAVCO database (Bartel, 2010) show a modern relative divergence of southwest-directed motion across the *ESRP* and into western Yellowstone (blue arrows) and northeast-directed motion (red arrows) mostly east and northeast of Yellowstone. All velocities relative to the fixed North American NAM 14 reference frame. (b) Map of the Teton-Yellowstone region showing the traditional extent of the Teton fault, a projected northern extension of the paleo-Teton fault (dashed red) from Brown et al. (2017) and Thigpen et al. (2021), and the intersection of fault projections with the Huckleberry Ridge (~2.06 Ma; purple) and Yellowstone-Lava Creek (0.6 Ma; green) caldera boundaries. The potential linkage with the active Hebgen Lake fault zone (HFLZ, dashed white) is also shown. Triangles denote positions of inverse thermal history models at Ranger Peak, Dome Mountain (Hoar, 2019), and those derived from Thigpen et al. (2021). Light brown bars represent trenching studies at Granite Canyon (Byrd, 1995), Buffalo Bowl (DuRoss et al., 2019), Steamboat Mountain (DuRoss et al., 2021), and Leigh Lake (Zellman et al., 2019). Numbers for GPS stations correspond with those assigned in Table 2. YNP, Yellowstone National Park. EGF, East Gallatin fault. ER, Eagles Rest. LL, Leigh Lake. M, Mount Moran. G, Grand Teton. S, Static Peak. GC, Granite Canyon. R, Rendezvous Peak. BB, Buffalo Bowl.

coincident with eastward migration of the mantle plume and its associated volcanism (Allmendinger, 1982; Anders et al., 1989; Pierce & Morgan, 1992). Key to this interpretation is the recognition that extensional fault systems north and south of the ESRP yield similar finite east-west extension magnitudes (15%, e.g., Anders et al., 1993; Janecke et al., 2000), which essentially requires that the ESRP has accommodated a similar magnitude of extension as those adjacent Basin and Range fault systems. The key implications of this, that extension is continuous across these relief transitions and that northern Basin and Range extension is linked to and potentially driven by the evolution of the ESRP (e.g., Rodgers et al., 2002), are critical to our understanding the genesis of this globally unique landscape.

Although these classic interpretations provide a fundamentally sound model of ESRP evolution to include development of the abrupt topographic breaks along the ESRP margin, it is less suitable for characterizing a similar transition between the modern Yellowstone plateau and the high relief of the adjacent Teton and East Gallatin Ranges (Figure 1b). In the classic model, the subdued relief of the ESRP relative to the Basin and Range mostly results from crustal subsidence that increases progressively moving southwest, which is attributed to post-emplacement cooling of mafic material in the crust (McQuarrie & Rodgers, 1998; Rodgers et al., 2002). However, the current position of the mantle plume beneath Yellowstone precludes crustal cooling and subsidence as a mechanism for denuding Teton and East Gallatin topography. Second, more recent thermochronology data indicates that motion on the Teton and East Gallatin normal faults (15–10 Ma) significantly pre-dates arrival of the mantle plume beneath Yellowstone at ~2 Ma and length-displacement scaling indicates that those faults likely extended across the area now occupied by the Yellowstone plateau (Brown et al., 2017; Helfrich et al., 2024; Hoar, 2019; Thigpen et al., 2021). If correct, this would imply that: (a) the Teton and East Gallatin footwall ranges should have been well established when the Yellowstone plume migrated into its present position, (b) the similar motion timing for the Teton and East Gallatin faults may result from a kinematic linkage of these two crustal

structures, or others, as has been posited by earlier studies (Christiansen, 2001; Ruppel, 1972), and (c) a mechanism(s) other than cooling-related subsidence must be invoked to explain the absence of modern Teton and East Gallatin footwall topography across Yellowstone.

Corroborating the existence of a longer paleo-Teton and/or East Gallatin fault system would impact our understanding of the interplay between caldera migration and the rapid removal of high mountain relief. Further, modern extension across this zone may indicate a need to reassess regional seismic hazard. However, direct evidence such as fault scarps or footwall topography linking active or recently active normal faults across the modern Yellowstone caldera remains limited (Christiansen and Blank, 1974a, 1974b, 1975). Here, we present the results of structural mapping of recently acquired LiDAR data, displacement analyses derived from structural mapping and thermochronologic analysis, and ground penetrating radar (GPR) surveying that reveal many active fault scarps within and adjacent to the Yellowstone caldera system. The mapped scarp data set includes a zone of north-south trending faults spanning the gap between the Teton and Gallatin Ranges. By integrating these results with geodetic and geophysical data and holistic models of normal fault growth and displacement accumulation, we interpret that these north-south fault segments likely represent the modern surface expression of a crustal-scale extensional zone between the Teton and East Gallatin faults. This would indicate the persistence or renewal of active east-west extension across the Yellowstone hotspot track. Furthermore, continued faulting through the otherwise undeformed rhyolite flows overlying the extensional zone may uniquely capture field evidence of the earliest and most rapid phase of crustal fault evolution, wherein isolated fault segments are actively propagating to re-establish the deformation zone of a crustal-scale normal fault, as predicted in fault growth models (e.g., Rotevatn et al., 2018).

2. Methods

2.1. Fault Scarp Mapping

Structural mapping was completed using two high-resolution LiDAR surveys (USGS, 2016; USGS, 2021). The Grand Teton and Yellowstone surveys were collected with a nominal pulse density of ~2 and ~22.8 pts m^{-2}, respectively. Last and single returns were extracted from the point cloud and mosaicked in ArcGIS Pro to generate a 1 m resolution bare-earth digital elevation model (DEM) and multidirectional hillshade surface for detailed structural mapping. Faults over the entirety of the survey area were mapped at their base (Figure 2), prioritizing only clear ground ruptures with distinct slope breaks. Other linear features, such as sackungen and near-fault lineaments formed and/or modified by erosion and glacial activity, were excluded (e.g., Figures 3a and 3b).

After identifying scarps, azimuthal trends (0°–180°) and segment lengths were measured in GIS software. The azimuthal distribution of the data set was used to separate scarps based on structural orientation into three main trends (N-S, NE-SW, E-W). Scarps were then compared with previously identified fault systems and assigned to a system based on their location and system trends. The geologic unit offset by each scarp was recorded. In addition, the nature of the interactions between the fault systems and the boundaries of the Huckleberry Ridge and Lava Creek calderas (e.g., positioned outside caldera boundary, truncated at caldera boundary, crosses caldera boundaries, intracaldera) was interpreted from the mapped relationships. Each of these attributes were incorporated into a feature class of all mapped ground ruptures, which is included in Data Sets S1–S4.

2.2. Fault Scarp Displacement Analysis

After completing the mapping, displacement analysis was undertaken on each fault scarp. Though swath analysis using intelligent tools has been successfully employed in the Teton region (Zhu et al., 2021) to measure displacements, we used a combined ArcGIS Pro and MATLAB workflow. As the results of traditional displacement analysis across geomorphic features (e.g., Hampel et al., 2021) are heavily dependent upon topographic profile location (Telbisz et al., 2013), topographic profiles were manually created for each fault in the data set. Locations were carefully selected based upon the clearest slope breaks and to avoid scarp-adjacent erosion and gullying (Figure 3b), as these measures ensure that the elevation differences on the hanging and footwall sides of the scarp realistically represent the true vertical separation. Coordinates for each profile were extracted at 1-m intervals to match the resolution of the DEM (Figure 3c). In MATLAB, regression lines were fitted to the ground surface (both above and below the fault) and the fault plane, calculating corresponding R-squared values and 95% confidence intervals for each fit (Figure 3d, and Data Sets S1–S4). Vertical separation was calculated as the elevation difference on either side of this best-fit plane, with surface uncertainties propagated through the calculation (Figure 3d). An example of this process is shown in Figure 3, and the full topographic profile analysis

10.1029/2024TC008752

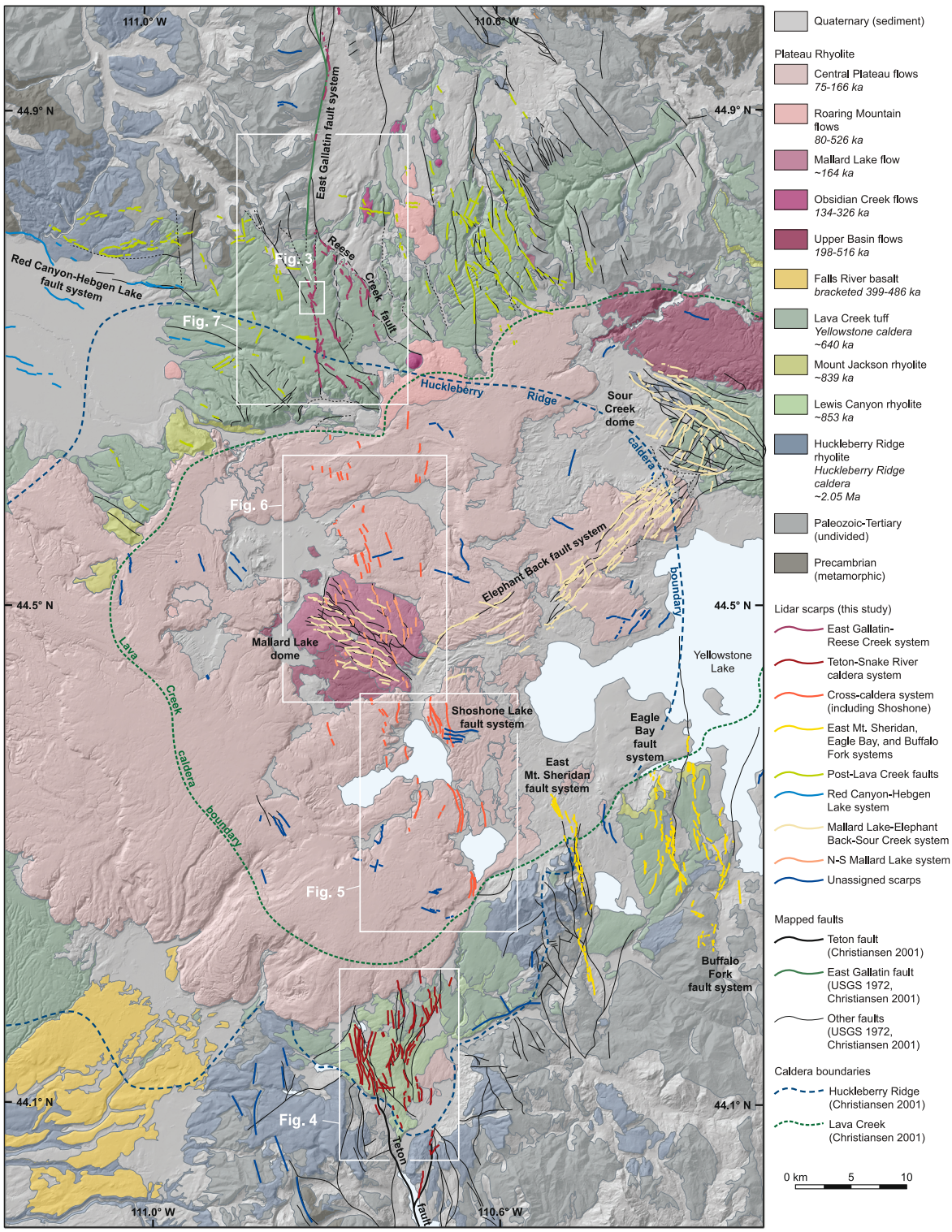

Figure 2. Hillshade map (generated in this study) of the study area overlain by a simplified geologic map of Christiansen (2001) showing major volcanic flow units, caldera boundaries, previously mapped faults, recently active north-south trending fault scarps mapped in the LiDAR data set (see explanation), and the overall trend of the extensional zone presented in this study. The locations of Figures 3–7 are shown (white boxes).

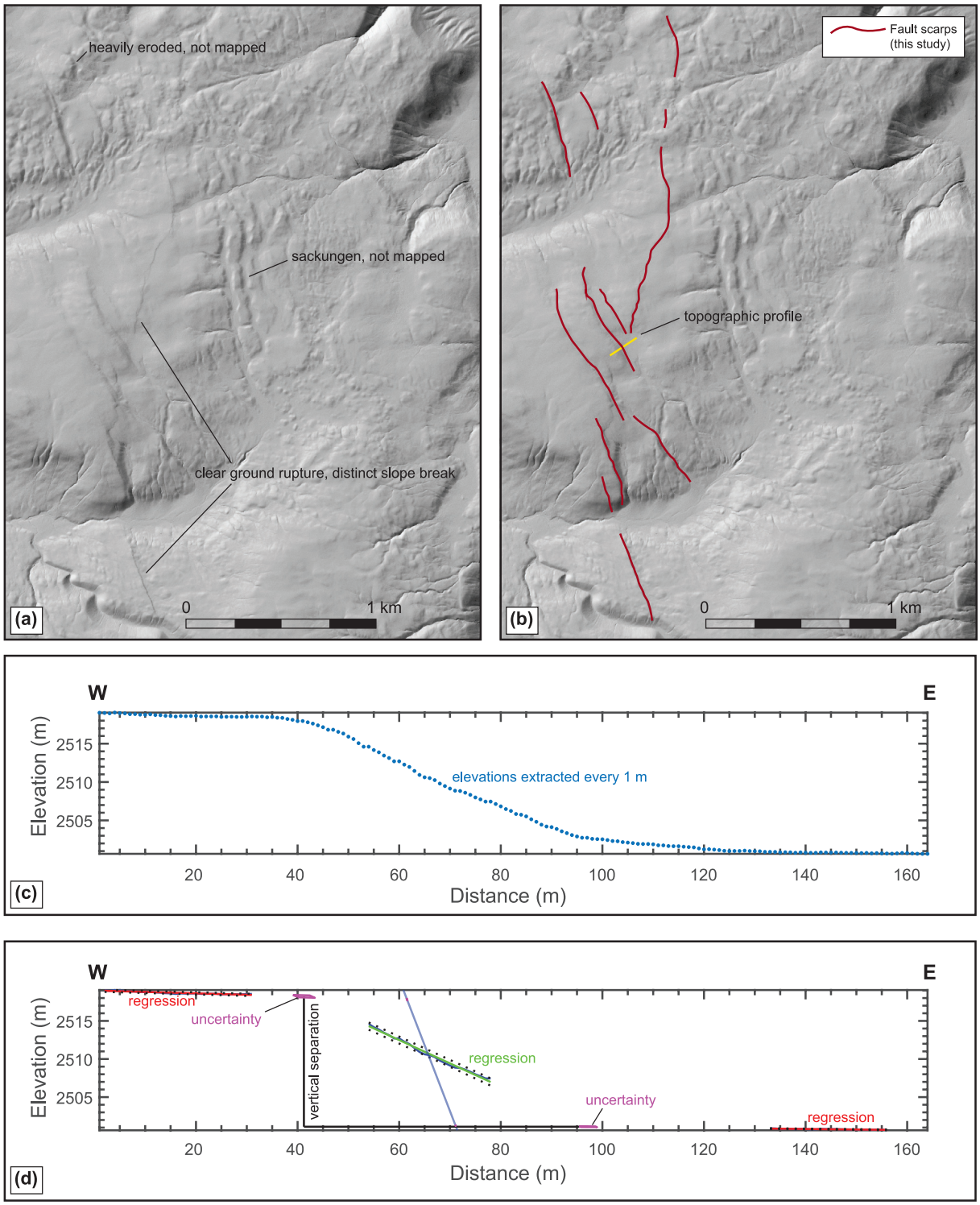

Figure 3. Methodology for mapping LiDAR features and analyzing displacement. (a) Uninterpreted hillshade image showing examples of mapped ground ruptures and unmapped features such as sackungen or heavily eroded areas where fault scarps could not be reasonably confirmed. (b) Interpreted hillshade of (a). Location of (a) and (b) indicated by blue box on Figure 7a. (c) Fault profile with points at 1-m intervals. (d) Results of fault displacement analysis where the red lines represent the fitted lines above and below the fault, and the green line represents the fault plane. Dashed lines represent the 95% confidence interval for each fit. The black lines indicate the vertical separation and horizontal extension of the fault, with the uncertainties represented by the magenta boxes. The blue line represents a hypothetical 60-degree fault plane.

for every transect is available in Data Sets S1–S4. Subsequently, throw, fault-plane slip, and slip (displacement) on a hypothetical 60° fault plane were computed (consistent with the conventions of Andersonian fault mechanics, Anderson, 1905) as well as constraints on Teton fault dip (Byrd et al., 1994; Haller et al., 1993; Helfrich et al., 2024).

2.3. Displacement Rate Derivation From LiDAR-Mapped Scarps

Displacement estimates were used to characterize fault architecture and linkage and to derive slip rates for 11 transects across the mapped N-S trending scarp systems (the dominant structural trend in the data set). Transects were positioned roughly orthogonal to structural trends to intercept as many fault scarps accommodating E-W extension as possible (Figures 4–7). Displacement estimates for each fault scarp (assumed 60° dip) were summed for each transect to obtain a total displacement for each along-strike segment of the structural system. In very few cases, a discernible elevation difference across the scarps was not clear in the topographic profile, and these were not included as part of the transect. All topographic profile locations which yielded displacements are shown in yellow on Figures 4–7.

Time-averaged displacement rates were calculated for each transect by dividing the total displacement by the crystallization age of the offset volcanic units (Table 1). This method allows total displacement to effectively be normalized for flow unit age. Due to complexities imparted by scarp erosion (e.g., Nash, 1980; Nash & Beaujon, 2006), the discrepancy between subsurface fault motion and ground rupture (Oglesby & Mai, 2012), and the potential for all rates to have been accelerated due to post-Pinedale glacial rebound (Liccardi & Pierce, 2008), results are interpreted to represent *only minimum constraints* on true displacement rates across this throughgoing extensional zone.

2.4. Displacement Estimates and Rates From Bedrock Structural Mapping and Thermochronology

As mapped LiDAR scarps record only recent displacement estimates, longer-term (>1 Ma) displacement estimates for the Teton, East Gallatin, and related faults were derived from mapped stratigraphic offsets (Love & Reed, 2000; Schroeder, 1972) or from integrated uplift and displacement modeling of thermochronology data (Brown et al., 2017; Thigpen et al., 2021). For the bedrock structural mapping, offset was either directly measured from published cross-sections (see references in Table 1) or interpreted from mapped structural relationships. Where possible, variable offset of units with different depositional or emplacement ages were used to develop slip magnitude and rate estimates for multiple temporal intervals (ex. Transect A-A′ shown in Figure 4c). Estimates of displacement magnitude, slip onset timing, and average displacement rate for thermochronology transects from Ranger Peak (RP) in the northern Teton Range and Dome Mountain (DM) in the Gallatin Range (Figure 1b) were produced following the methodology and parameters of Thigpen et al. (2021). Displacement magnitude, timing and displacement rates for the Mount Moran, Static Peak, and Rendezvous Mountain transects in the Teton Range were derived directly from the inverse temperature-time models of Thigpen et al. (2021). The details of all displacement estimates and rate interpretations, including input data and required assumptions, are included in Data Sets S1–S4.

2.5. Ground-Penetrating Radar (GPR) Survey

As the LiDAR-mapped fault scarps are discontinuous on the surface, a single GPR survey was acquired to test for the presence of fault segments at depth across an area where surface expressions may be obscured by deposition or glacial activity. The GPR survey was acquired using 50 MHz antennae with 32,000 stacks per survey point and a spacing of 0.5 m between survey points along the 750 m line. Post-acquisition processing included an amplitude gain control of 200 ms and a bandpass filter. Although this survey only covers a small part of the study area, it is included here to: (a) confirm that mapped features interpreted as fault scarps manifest at depth, and (b) assess the degree to which surface processes act to remove or obscure active faults and thereby confirm that this analysis offers minimum estimates of true displacement rates.

3. Results

3.1. Scarp Mapping

Numerous normal-sense fault scarp segments (n = 1,039) were identified across the Yellowstone study area. A summary of the mapped scarp segments is shown in Figure 2, and all scarp segments are included in the GIS file in

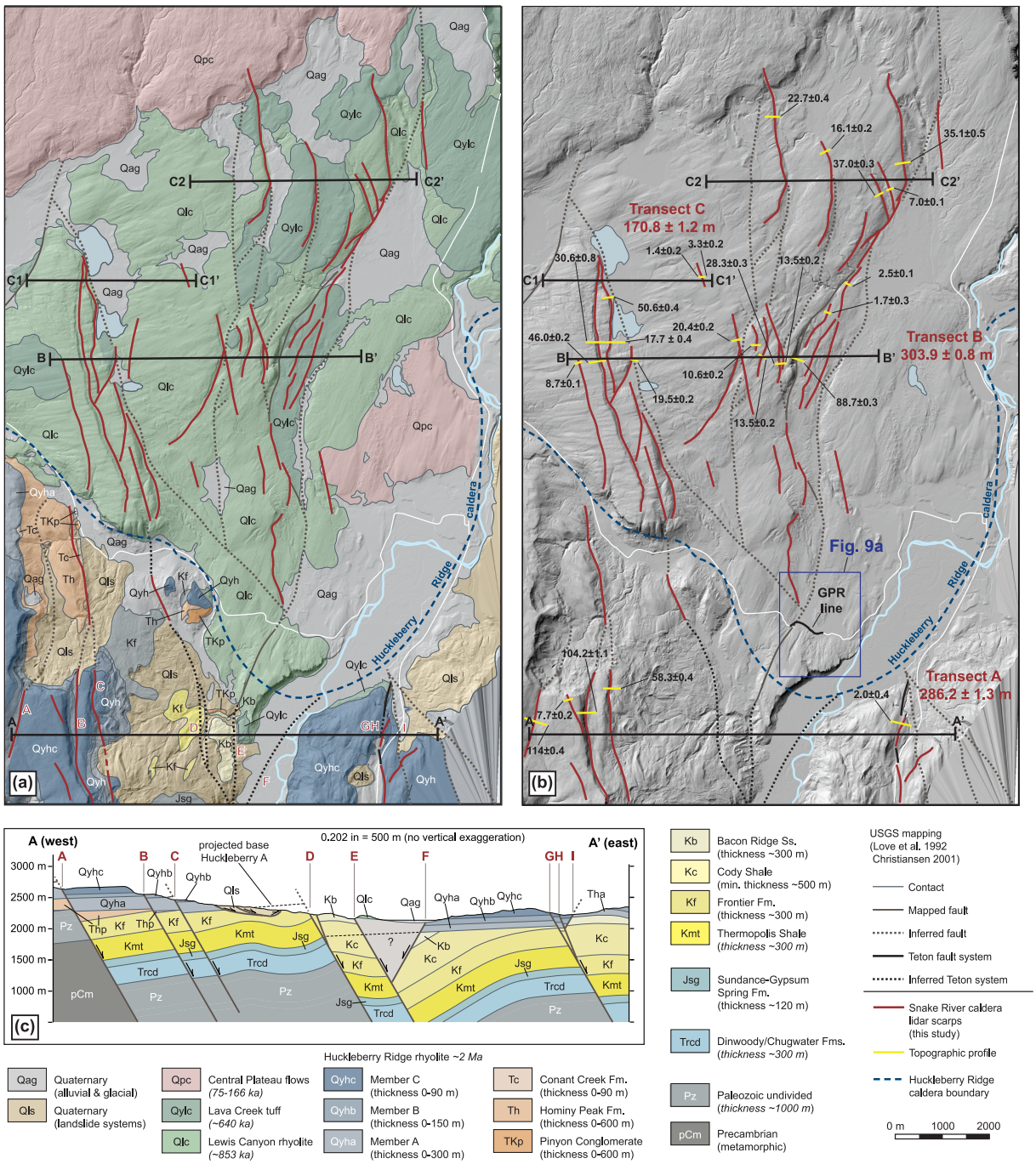

Figure 4. (a) Hillshade map of southern Yellowstone and the northern Tetons overlain with simplified geology of Love et al. (1992) and Christiansen (2001). Mapped Quaternary faults (gray dashed lines) and LiDAR features mapped by this study (red lines) are shown. Section lines A-A′, B-B′, C1-C1′, and C2-C2′ cross structural features offsetting the Huckleberry Ridge, Lava Creek tuff, and Lewis Canyon rhyolite. (b) Hillshade map of same area shown in (a) with estimated displacements of individual segments (black text) across manually selected topographic profiles (yellow lines). Total displacements reported in Table 1 are the sum of estimated vertical slip across all scarps along the section lines assuming a fault dipping 60°. Estimates are shown in Table 1. (c) Transect A-A′, immediately south of the Huckleberry Ridge caldera boundary, yields summed LiDAR scarp displacements of 66.2 ± 5.3 m and summed cross section displacements for the Huckleberry Ridge flows and the Cretaceous-Paleozoic units of 1,179 ± 94 and 3,979 ± 318 m, respectively.

Data Sets S1–S4. The majority of the mapped scarp segments (n = 588) trend approximately north-south, with a lesser number trending in other orientations (Figures 8a and 8b). Many of the mapped scarps correspond to previously identified fault systems, including the Buffalo Fork (n = 37, Christiansen, 2001; Love &

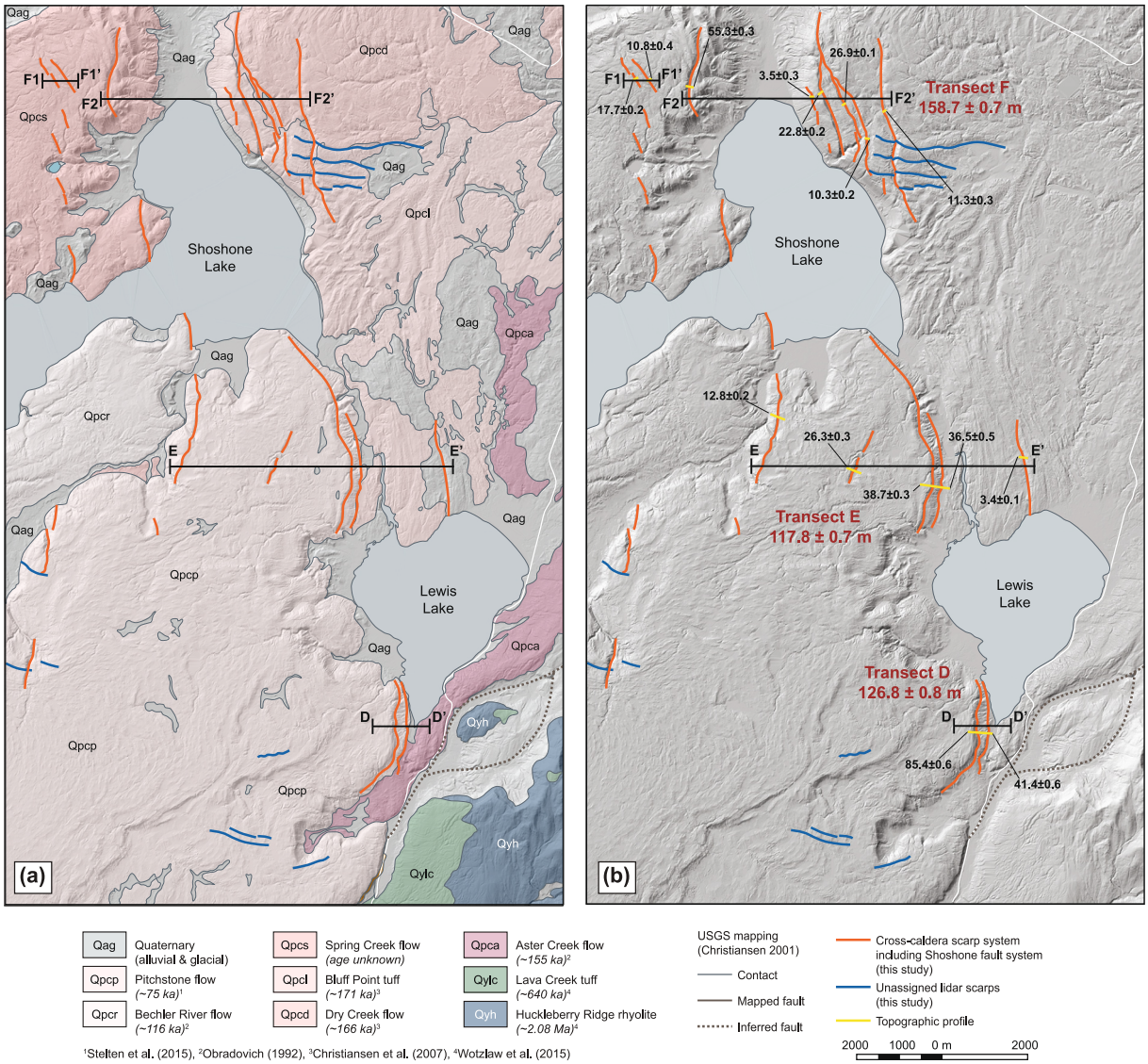

Figure 5. (a) Hillshade map of south-central Yellowstone overlain with simplified geology of Love et al. (1992) and Christiansen (2001). Mapped Quaternary faults (gray dashed lines) and LiDAR features mapped by this study (orange lines) are shown. Transect lines D-D′, E-E′, F1-F1′, and F2-F2′ intersect scarps preserving offset within the Pitchstone and Bluff Point/Dry Creek tuffs. (b) Hillshade map of same area shown in (a) with estimated displacements of individual segments (black text) across manually selected topographic profiles (yellow lines). Total displacements reported in Table 1 are the sum of estimated vertical slip across all scarps along the section lines assuming a fault dipping 60°. Estimates are shown in Table 1.

Keefer, 1975), Eagle Bay (n = 107, Locke et al., 1992; Witkind, 1975) and East Mt. Sheridan fault systems (n = 56, Christiansen, 1974) south of Yellowstone Lake (Figure 2). Scarps representing the East Mt. Sheridan fault system extend ~10 km into the Lava Creek caldera but abruptly terminate, with no evidence of further northern extension. Scarps associated with the Eagle Bay and Buffalo Fork fault systems are also mostly truncated at or near the inferred position of the Lava Creek caldera boundary (e.g., Christiansen, 2001), though seismic reflection profiling of Yellowstone Lake shows evidence that the Eagle Bay fault system may extend across the lake and potentially merge with the Elephant Back fault system (e.g., Morgan et al., 2003, 2007).

The mapped scarp segments also represent recent fault motion associated with the Mallard Lake (Case, 1997; Christiansen, 1974; Christiansen & Blank, 1974a, 1974b) and Sour Creek resurgent domes (Christiansen & Blank, 1975), and the Elephant Back fault system (Christiansen, 2001) that links them (Figure 2). North of the Lava Creek caldera, mapped scarps align with the Reese Creek fault system (Haller et al., 1993; Ruppel, 1972; Wilson, 1934) and, critically, a relatively continuous southern extension of the East Gallatin fault system (Haller

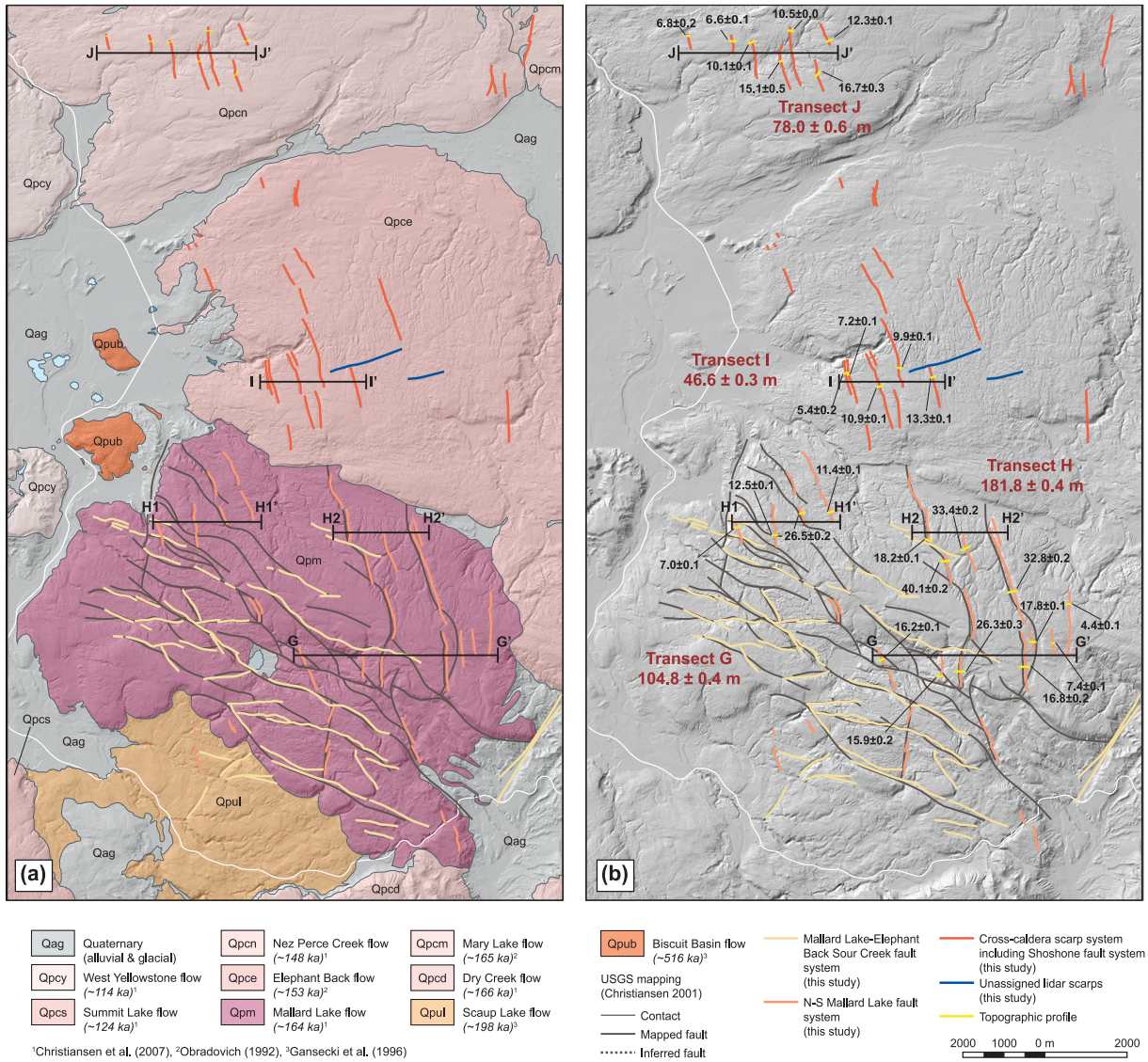

Figure 6. (a) Hillshade map of north-central Yellowstone overlain with simplified geology of Love et al. (1992) and Christiansen (2001). Mapped Quaternary faults (gray dashed lines) and LiDAR features mapped by this study (orange lines) are shown. Transect lines G-G′, H1-H1′, H2-H2′, I-I′, J1-J1′, and J2-J2′ positioned to intersect fault segments cutting the Mallard Lake, Elephant Back, and Nez Perce Creek flows. (b) Hillshade map of same area shown in (a) with estimated displacements of individual segments (black text) across manually selected topographic profiles (yellow lines). Total displacements reported in Table 1 are the sum of estimated vertical slip across all scarps along the section lines assuming a fault dipping 60°. Estimates are shown in Table 1 (Gansecki et al., 1996; Obradovich, 1992).

et al., 1993; Christiansen, 2001; Figures 2 and 7). Multiple scarps (n = 231) also overlap with the previously interpreted post-Lava Creek fault system(s) north of the Lava Creek caldera (Christiansen, 2001; Christiansen & Blank, 1974a, 1974b; Figure 2) and the Red Canyon-Hebgen Lake fault system (n = 15, Doser, 1985; Witkind, 1964) in northwestern Yellowstone. Both the Red Canyon-Hebgen Lake and post-Lava Creek systems lie mostly outside of the caldera boundaries, though minor faulting interpreted as part of both systems is recognized inside the position of the Huckleberry Ridge caldera in northwestern Yellowstone (Figure 2).

In central Yellowstone, multiple north-south trending extensional scarp groups were identified offsetting flows of the Central Plateau Group, including the Pitchstone flow (~75 ka, Stelten et al., 2015) north and south of Mallard Lake dome (Figures 2, 5, and 6). On the southern side of the Lava Creek caldera, this cross-caldera fault system, which includes part of the Shoshone Lake fault system (n = 37, Christiansen, 1974; Love & Keefer, 1975), is positioned between scarps of the Snake River caldera (e.g., Christiansen, 2001; Figures 2 and 5) and Mallard Lake dome systems. Importantly, these scarp groups collectively form a north-south trending extensional zone that

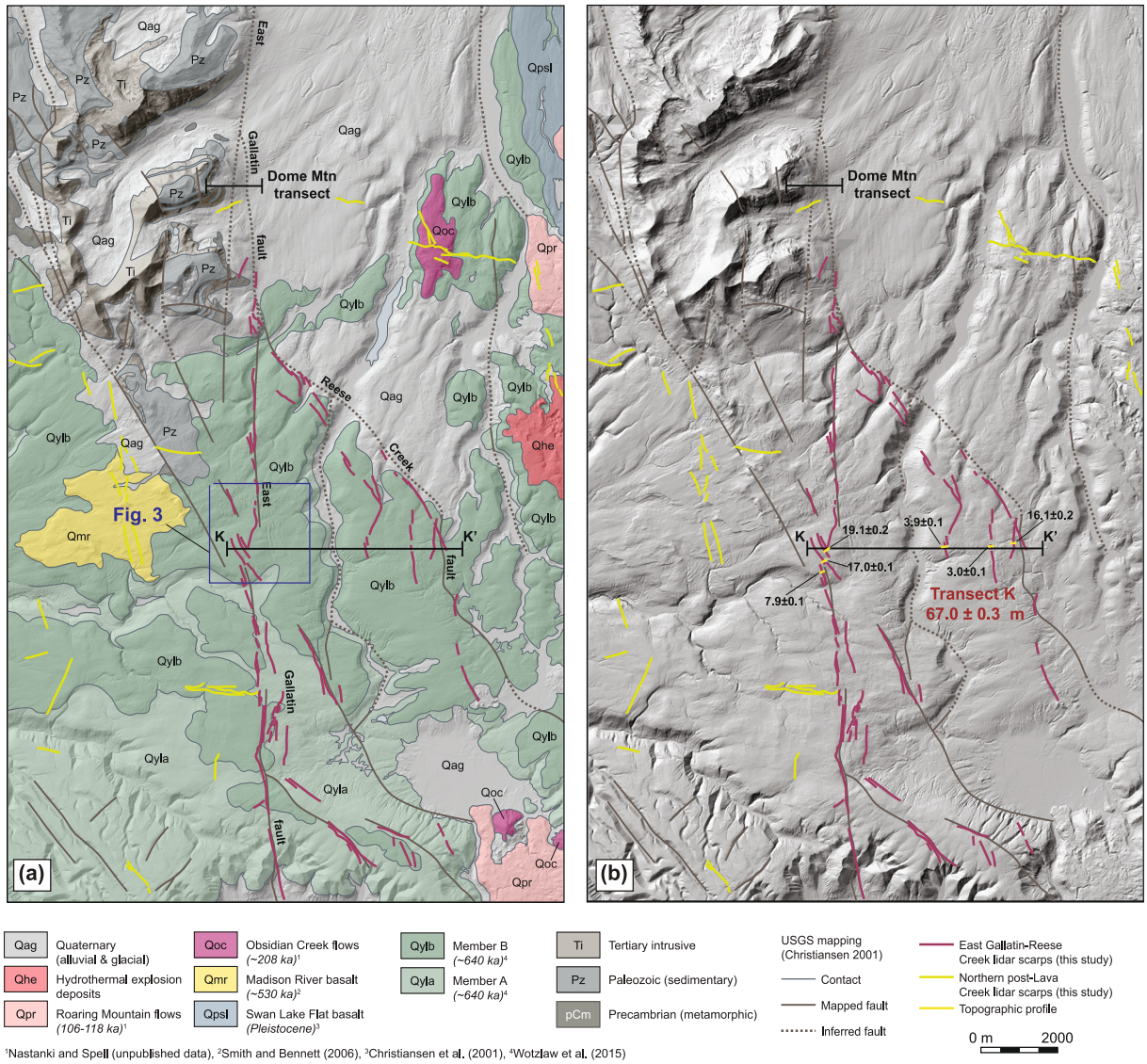

Figure 7. (a) Hillshade map of northern Yellowstone and the southern Gallatin Range overlain with simplified geology of Love et al. (1992) and Christiansen (2001). Mapped Quaternary faults (gray dashed lines) and LiDAR features mapped by this study (orange lines) are shown. Transect K-K′ crosses fault segments across the Lava Creek tuff (members A and B). The location of the Dome Mountain thermochronologic transect of Hoar (2019) is also shown. (b) Hillshade map of same area shown in (a) with estimated displacements of individual segments (black text) across manually selected topographic profiles (yellow lines). Total displacements reported in Table 1 are the sum of estimated vertical slip across all scarps along the section lines assuming a fault dipping 60°. Estimates are shown in Table 1 (Smith & Bennett, 2006; Wotzlaw et al., 2015).

aligns broadly with both the Teton and East Gallatin faults and represents the only continuous or semi-continuous fault system that spans the entirety of both the Huckleberry Ridge and Lava Creek calderas (Figure 2).

3.2. Displacement Analysis From LiDAR Mapping

In southern Yellowstone, displacement magnitudes were calculated for three transects crossing mapped LiDAR scarps (Figures 4a and 4b). For the southernmost transect (A-A′), displacement estimates were also calculated for interpreted offset of the Huckleberry Ridge flows and Cretaceous-Paleozoic units, respectively, based on structural cross-section analysis of previous detailed mapping (e.g., Christiansen, 2001; Love et al., 1992). Transect A-A′, immediately south of the Huckleberry Ridge caldera boundary, yields a summed LiDAR scarp displacement of 286.2 ± 1.3 m across the 2.06 ± 0.004 Ma Huckleberry Ridge flow (Lanphere et al., 2002). Stratigraphic offset of the mapped Huckleberry Ridge fault system (Love et al., 1992) yields an estimated displacement of 1,179 ± 94 m.

Table 1
Estimated Displacement Magnitudes, Fault Motion Onset Timing, and Average Displacement Rates for Along-Strike Positions on the Teton-Yellowstone-East Gallatin Fault System

Locality	Units offset	Slip onset (ka or Ma)	Estimated displacement (km)	Avg. slip rate (km Myr^{-1})	Along-strike position (km)	Method	Reference
Dome Mtn.	Pre-Cretaceous	14.3 ± 1.8 Ma	12.2 ± 4.1 km	0.85 ± 0.45	171.1	AHe transect	Hoar (2019), this study
Transect K-K′	Qylcb/a	<640 ka	67.0 ± 0.3 m	0.10 ± 0.00	159.9	Lidar mapping	This study
Transect J-J′	Qpcn	<148 ka	78.0 ± 0.6 m	0.53 ± 0.00	152.7	Lidar mapping	This study
Transect I-I′	Qpce	<153 ka	46.6 ± 0.3 m	0.30 ± 0.00	144.0	Lidar mapping	This study
Transect H-H′	Qpm	<164 ka	181.8 ± 0.4 m	1.12 ± 0.00	139.6	Lidar mapping	This study
Transect G-G′	Qpm	<164 ka	104.8 ± 0.4 m	0.64 ± 0.00	135.6	Lidar mapping	This study
Transect F-F′	Qpcd	<166 ka	158.7 ± 0.7 m	0.96 ± 0.00	126.8	Lidar mapping	This study
Transect E-E′	Qpcp, Qpcl	75–171 ka	117.8 ± 0.7 m	1.13 ± 0.45	121.7	Lidar mapping	This study
Transect D-D′	Qpcp	<75 ka	126.8 ± 0.8 m	1.69 ± 0.01	111.6	Lidar mapping	This study
Transect C-C′	Qylc, Qlc	640-853 ka	170.8 ± 1.2 m	0.23 ± 0.04	108.4	Lidar mapping	This study
Transect B-B′	Qylc, Qlc	640-853 ka	303.9 ± 0.8 m	0.42 ± 0.06	98.4	Lidar mapping	This study
Transect A-A′	Qyhc	<2.06 ± 0.004 Ma	286.2 ± 1.3 m	0.14 ± 0.00	88.8	Lidar mapping	This study
	Qyhc	<2.06 ± 0.004 Ma	1,179 ± 94 m	0.57 ± 0.02	88.8	Stratigraphic offset	Love et al. (1992), This study
	Pre-Qyhc	9.5 ± 0.5 Ma	3,979 ± 318 m	0.42 ± 0.06	88.8	Stratigraphic offset	Love et al. (1992), This study
Ranger Peak	Basement	9.0 ± 1.0 Ma	10.0 ± 2.8 km	1.11 ± 0.49	74.9	AHe transect	This study
Eagles Rest Peak	Basement	9.0 ± 1.0 Ma	9.2 ± 1.2 km	1.02 ± 0.28	70.9	AHe transect	This study
Signal Mountain	Qyhc	2.06 ± 0.004 Ma	2.5 ± 0.4 km	1.20 ± 0.19	65.7	Tilting of Qyhc	This study
Moran Bay	Post-glacial (?)	14.6–13.5 ka	26.6 ± 2.7 m	1.14 ± 0.11	63.4	Lidar mapping	Gilbert et al. (1983)
Mt. Moran	Basement	9.5 ± 0.5 Ma	11.9 ± 0.6 km	1.25 ± 0.14	60.8	AHe transect	Hampel et al. (2021)
Pm1 Jenny Lake	Lateral moraine	14.6–13.5 ka	26.6 ± 2.7 m	1.89 ± 0.28	53.6	Lidar mapping	Thigpen et al. (2021)
Pm3 Phelps Lake	Lateral moraine	14.6–13.5 ka	14.6 ± 1.5 m	1.04 ± 0.15	43.8	Lidar mapping	Hampel et al. (2021)
Static Peak	Basement	15.4 ± 0.6 Ma	11.4 ± 0.6 km	0.74 ± 0.07	43.8	AHe transect	Hampel et al. (2021)
Pf10 Granite Canyon	Post-glacial (?)	14.6–13.5 ka	11.9 ± 0.6 m	0.85 ± 0.08	37.4	Lidar mapping	Thigpen et al. (2021)
Rendezvous Mtn.	Basement	8.5 ± 1.5 Ma	11.2 ± 1.0 km	1.32 ± 0.43	34.0	AHe transect	Hampel et al. (2021)
Pf12 Buffalo Bowl	Post-glacial (?)	14.6–13.5 ka	12.0 ± 1.2 m	0.85 ± 0.12	34.0	Lidar mapping	Thigpen et al. (2021)
Open-Phillips Canyon	Paleozoic	8.5 ± 1.5 Ma	4.6 ± 0.4 km	0.54 ± 0.18	26.0	Stratigraphic offset	Hampel et al. (2021)
Jackson 24K	Upper Cretaceous	8.5 ± 1.5 Ma	~0.30 km	0.04 ± 0.01	12.0	Stratigraphic offset	Schroeder (1972)
Hoback Junction	Upper Cretaceous	8.5 ± 1.5 Ma	~0.09 km	0.01 ± 0.00	1.0	Stratigraphic offset	Love & Albee (1972, 2004)
S. termination	n/a	8.5 ± 1.5 Ma	~0.00 km	n/a	0.0	n/a	Schroeder (1974)
							Schroeder (1974)

Note. The southern termination of the Teton fault system represents the reference starting position (0.0 km) for along-strike positions. Post-glacial onset age based on Pinedale end stage moraines of Liccardi and Pierce (2008).

Across Cretaceous-Paleozoic units since Teton fault slip onset at 9.5 ± 0.5 Ma (Thigpen et al., 2021), 3,979 ± 318 m of displacement can be accounted for along transect A-A′. Dividing the total displacement by the Huckleberry Ridge age along the A-A′ transect yields a slip rate of 0.14 ± 0.00 km Ma^{-1} (<0.01; Table 1, Figure 4c, Tables S3 and S4 in Supporting Information S1) since 2.06 Ma. Transects B-B′ and C-C′, which offset the 853 ka Lewis Canyon and 640 ka Lava Creek flows in southern Yellowstone, yield displacement estimates of 303.9 ± 0.8 and 170.8 ± 1.2 m, respectively (Figure 4b). Displacement rates are thus 0.42 ± 0.06 and 0.23 ± 0.04 km Ma^{-1} across the B-B′ and C-C′ transects. Transect D-D′, which offsets only the 75 ka Pitchstone flow, yields a displacement estimate of 126.8 ± 0.8 m and a rate of 1.69 ± 0.01 km Ma^{-1} (Figure 5). Transect E-E′ offsets both the 75 ka Pitchstone flow and the 171 ka Bluff Point tuff. Displacement across this transect totals 117.8 ± 0.7 m and the slip

Table 2
University NAVSTAR Consortium (UNAVCO) GPS Stations Across the Yellowstone Caldera

Station #	Station name	Rate (mm yr^{-1})	Azimuth
1	YNPPromtryWY2005	0.36	93.2
2	GrantT944GWY2012	0.81	198.0
3	OFW2_EBRY_WY2003	1.49	233.4
4	LKWY_EBRY_WY1996	0.74	215.6
5	WLWY_EBRY_WY1999	0.79	170.5
6	YNPCanyon_WY2005	1.15	157.0
7	NRWY_EBRY_WY2003	2.69	160.0
8	ShoshoneRvWY2006	0.44	118.3
9	Chief_Joseph_WY_	0.59	110.0
10	YNPPantherWY2008	1.48	47.5
11	MAWY_EBRY_WY1998	1.14	64.6
12	YNPSlough_WY2005	0.77	67.1
13	YNP_NEEnt_MT2005	0.93	85.7
14	HLF_KirkwdMT2008	1.56	47.0
15	YNP_Bacon_MT2008	1.41	42.0
16	HLF_WapitiMT2007	1.12	43.9
17	HLFContourMT2007	1.32	181.0
18	BBID_EBRY_ID2002	2.30	218.0
19	YNPFishCrkID2007	2.65	222.6
20	HLFIslParkID2005	2.78	214.3
21	HLFSawtellID2007	3.48	222.0
22	YNPWestYelMT2005	2.70	202.2
23	HLFHnrysLkID2005	2.54	205.9
24	GTNPGrassyWY2007	1.42	209.0
25	GTNPMoose_WY2007	1.74	206.0
26	YNPGrandTgWY2010	2.11	210.0
27	Driggs	2.17	214.5
28	GTNPUhlHilWY2007	1.05	229.6
29	SWY_EBRY_WY2001	1.14	219.70

Note. Station # corresponds to those shown on Figure 1b. Rates at each station are provided in mm yr^{-1}, and azimuth indicates motion direction.

rate is 1.13 ± 0.45 km Ma^{-1}. Transect F-F′ yields a displacement estimate of 158.7 ± 0.7 m for offsets of the 166 ka Spring Creek and Dry Creek flows and a rate of 0.96 ± 0.00 km Ma^{-1} (Figure 5). Transects G-G′ and H-H′ yield displacement estimates of 104.8 ± 0.4 and 181.8 ± 0.4 m, respectively, for offsets on approximately north-south trending scarps cutting the 164 ka Mallard Lake flow. Resulting rates on these transects are 0.64 ± 0.00 and 1.12 ± 0.00 km Ma^{-1}. Transects I-I′ and J-J′ yield displacement estimates of 46.6 ± 0.3 and 78.0 ± 0.6 m for offsets across the 153 ka Elephant Back and 148 ka Nez Perce Creek flows, respectively (Figure 6), for displacement rates of 0.30 ± 0.00 and 0.53 ± 0.00 km Ma^{-1}. Lastly, Transect K-K′ yields a displacement estimate of 67.0 ± 0.3 m across the A and B members of the Lava Creek flows immediately south of the Gallatin Range in northern Yellowstone (Figure 7). Northernmost displacement rates are thus estimated to be 0.10 ± 0.00 km Ma^{-1}. All displacements and rates are provided in Table 1.

3.3. Ground Penetrating Radar (GPR) Survey

The GPR survey was positioned on an east-west section of Grassy Lake Road between two zones where multiple ground-rupturing north-south fault scarps are recognized in the DEM but there is no evidence of surface faulting (Figures 4 and 9). In the processed subsurface section line, multiple normal faults offset a sequence of near surface reflector packages. Faults were interpreted where stratal geometries truncated, where reflectors bent sharply upwards, or where subsurface diffractions were clear. Sedimentary packages (distinct packages bound by high-reflectivity surfaces) that show abrupt thickness changes from footwall to hanging wall are interpreted as synkinematic and are expressed both across single faults and across multi-strand fault systems, similar to the architecture observed in near-surface trenches across the Teton and related faults (e.g., DuRoss et al., 2019, 2021). Most faults interpreted in the section but not present as a surface rupture preserve offsets of 0.5–1.5 m (assuming a wet sand velocity of 0.08 m ns^{-1}), however, the multi-segment fault zone provisionally correlated with the major ground rupturing scarp expressed just north in the DEM and exhibiting ∼8 m of vertical separation (lineament A, Figure 9a) preserves an offset of ∼7.1 m (∼88 ns one-way time) in near-surface sediments.

3.4. Displacement Analysis for the Teton and East Gallatin Faults From Bedrock Mapping and Thermochronology

Teton fault displacement was calculated at Steamboat Mountain and Signal Mountain based on the detailed bedrock mapping of Love et al. (1992) and was derived from modeling of footwall thermochronology transects at RP in the northern Tetons and the DM transect in the southern Gallatin Range (Hoar, 2019). All results are summarized in Table 1 along with rates constrained by other studies. Input thermochronology data and QTQt model results are included in Supporting Information S1.

At Steamboat Mountain, offset on the ∼2.06 Ma Huckleberry Ridge tuff, determined from cross-section analysis of the bedrock mapping (Figure 4c; Goldsby et al., 2023; Love et al., 1992), is interpreted to be 1,179 ± 94 m. Older displacement on the pre-Huckleberry units in the same cross-section is interpreted to be 3,979 ± 318 m. Calculated average displacement rates, which assume a fault slip onset at ∼2.06 and 9.5 ± 0.5 Ma for the Huckleberry and pre-Huckleberry units, respectively, are 0.57 ± 0.02 and 0.42 ± 0.06 km Ma^{-1}. The fault slip onset time for pre-Huckleberry units is derived from fault slip onset estimates for the Mount Moran inverse thermal history model (Thigpen et al., 2021).

Inverse thermal history modeling of thermochronology data for the RP transect along the Teton fault and the DM transect along the East Gallatin fault yields total cooling estimates of 79 ± 21 and 94 ± 28°C, respectively

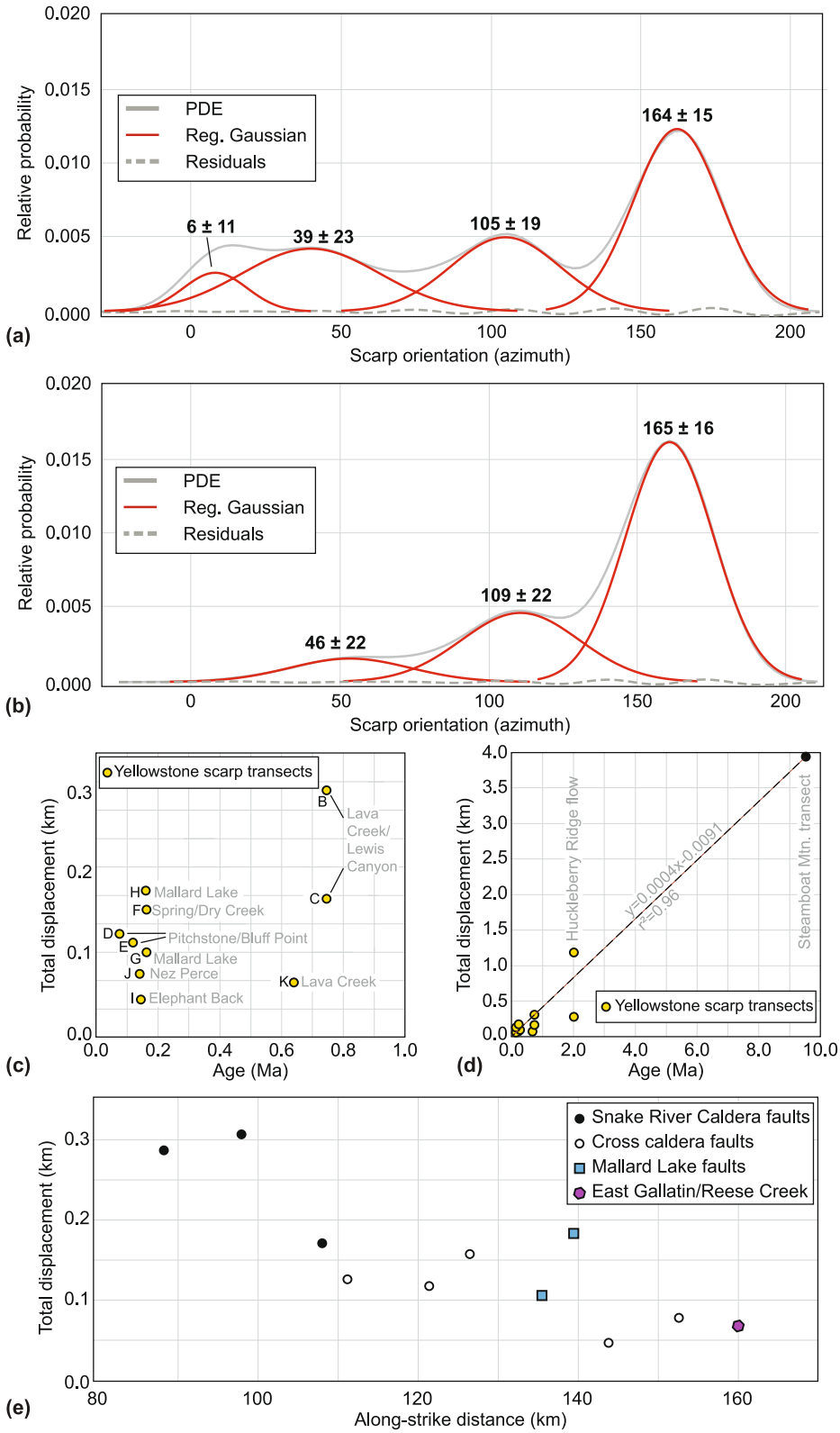
(a)
Relative probability
PDE
Reg. Gaussian
Residuals
6 ± 11
39 ± 23
105 ± 19
164 ± 15
Scarp orientation (azimuth)
(b)
Relative probability
PDE
Reg. Gaussian
Residuals
46 ± 22
109 ± 22
165 ± 16
Scarp orientation (azimuth)
(c)
Yellowstone scarp transects
Total displacement (km)
Age (Ma)
B Lava Creek/ Lewis Canyon
C
H Mallard Lake
F Spring/Dry Creek
D
E Pitchstone/Bluff Point
G Mallard Lake
J Nez Perce
K Lava Creek
I Elephant Back
(d)
Total displacement (km)
Age (Ma)
Huckleberry Ridge flow
y=0.0004x-0.0091
r²=0.96
Steamboat Mtn. transect
Yellowstone scarp transects
(e)
Total displacement (km)
Along-strike distance (km)
Snake River Caldera faults
Cross caldera faults
Mallard Lake faults
East Gallatin/Reese Creek

Figure 8.

(Figures S1 and S2 in Supporting Information S1), for the lowest elevation sample on each transect. Integration of a modeled geothermal gradient of 32.0°C km^{-1} for RP and 30.5°C km^{-1} for DM, which are derived from the modeled surface heat flow data of Blackwell and Richards (2004) and following the methodology detailed in Thigpen et al. (2021), yields a total footwall uplift magnitude of 2.5 ± 0.7 km for RP and 3.0 ± 1.0 km for DM (thermal model details included in Supporting Information S1). Using the footwall uplift/total displacement relationship of Thigpen et al. (2021) yields total displacements 10.0 ± 2.8 km for RP and 12.2 ± 4.1 km for DM. Using fault slip onsets of 9.9 ± 3.8 Ma at RP and 14.3 ± 1.8 Ma at DM, yields average displacement rates of 1.11 ± 0.49 and 0.85 ± 0.45 km Ma^{-1}, respectively.

4. Discussion

4.1. Quaternary-Modern Yellowstone Extension

The analysis presented here yields multiple groups of recently active and genetically-linked scarp groups in the Teton-Yellowstone region. Many of these mapped scarps are associated with previously mapped fault groups, including the Elephant Back, Shoshone Lake, East Mount Sheridan, Eagle Bay, Buffalo Fork, Red Canyon-Hebgen Lake, and Reese Creek fault systems. Mapped scarps also include those associated with modern faulting and volcanic activity around the Mallard Lake and Sour Creek domes (Figure 2). However, our scarp mapping also highlights a previously unmapped fault scarp system that extends across the modern Yellowstone caldera and spatially aligns with the East Gallatin fault in the north (Figures 2 and 7) and the Snake River caldera faults in the south (Figures 2 and 4). This ∼10–15 km wide scarp system accommodates east-west extension across multiple Yellowstone volcanic units of varying ages (∼75–853 ka; Table 1). At along-strike positions where these normal faults offset single flow units, the age of the flow unit and the total magnitude of preserved displacement are positively correlated (Figures 8c and 8d), suggesting that east-west extension has likely persisted at least since emplacement of the oldest flow (i.e., Lewis Canyon, ∼853 ka). Although our LiDAR analysis emphasizes surface scarps, GPR results (Figure 9) indicate offset at depth even where surface expression is obscured (either by deposition or erosional modification), thus the total displacement accommodated by this fault system is likely higher than that evidenced by ground ruptures alone. Moreover, subsurface offsets being roughly equivalent to surface offsets on aligned fault scarps indicates that seemingly discontinuous ground ruptures may be linked complexly across the caldera.

4.2. Linking Teton, Yellowstone, and East Gallatin Extensional Faulting

Multiple studies have either interpreted direct linkages between the main Teton fault system and faults offsetting the Yellowstone flows or have proposed linkage of now-removed paleo-faults across the Yellowstone caldera track (e.g., Brown et al., 2017; Byrd et al., 1994; Christiansen, 2001; Love et al., 1992; Ruppel, 1972; Smith et al., 1993; Thigpen et al., 2021). However, identifying more direct structural, geomorphic, or geophysical evidence that the extensional zone originally extended and/or persists across the caldera track has proved challenging.

In the northern Tetons, the fault is traditionally interpreted to follow northern Jackson Lake and the Snake River Valley east of Steamboat Mountain, beneath thick layers of Quaternary alluvium adjacent to the Huckleberry Ridge caldera margin (Figure 4; Love et al., 1992). Despite the alluvial cover, isolated exposures of Cretaceous sedimentary and Quaternary volcanic units demonstrate that multiple extensional faults, including the down to the west Snake River fault, are kinematically linked to the Teton fault between the modern range front and Steamboat Mountain (transect A-A′, Figure 4). Based on our structural analysis of previous detailed mapping here (Christiansen et al., 1978; Love et al., 1992; Ostenaa et al., 1993; Richmond, 1973), those faults (A-I on transect

Figure 8. Azimuthal orientation distribution for LiDAR-derived ground ruptures mapped in this study. (a) Unweighted and (b) weighted by scarp length. Fault sets were divided by the troughs in the unweighted azimuthal trend (0–12.3 or 133.5–180 is NS; 12.3 to 74.7 is NE; 74.7 to 133.5 is EW) and the regionally significant N-S trending scarps ($n = 588$) were isolated and used for displacement analysis. Peak values include 1σ uncertainty. All azimuths are included as part of the GIS file in Supporting Information S1. (c) At along-strike positions where these normal faults offset single flow units, the age of the flow unit and the total magnitude of preserved displacement are positively correlated, suggesting that east-west extension has likely persisted at least since emplacement of the oldest flow (i.e., Lewis Canyon, ∼853 ka). (d) Similar figure to (a) but includes the age and total displacement relationships for the Yellowstone scarps in (a), the Huckleberry Ridge offsets between the Tetons and Yellowstone, and the cross-section transect (Figure 4) in the vicinity of Steamboat Mountain. (e) Parabolic distributions of along-strike displacement measured across transects A-K (alphabetical from left to right) in this study provide evidence that the faults spanning the Yellowstone caldera are accumulating displacement as part of an evolving and throughgoing extensional system.

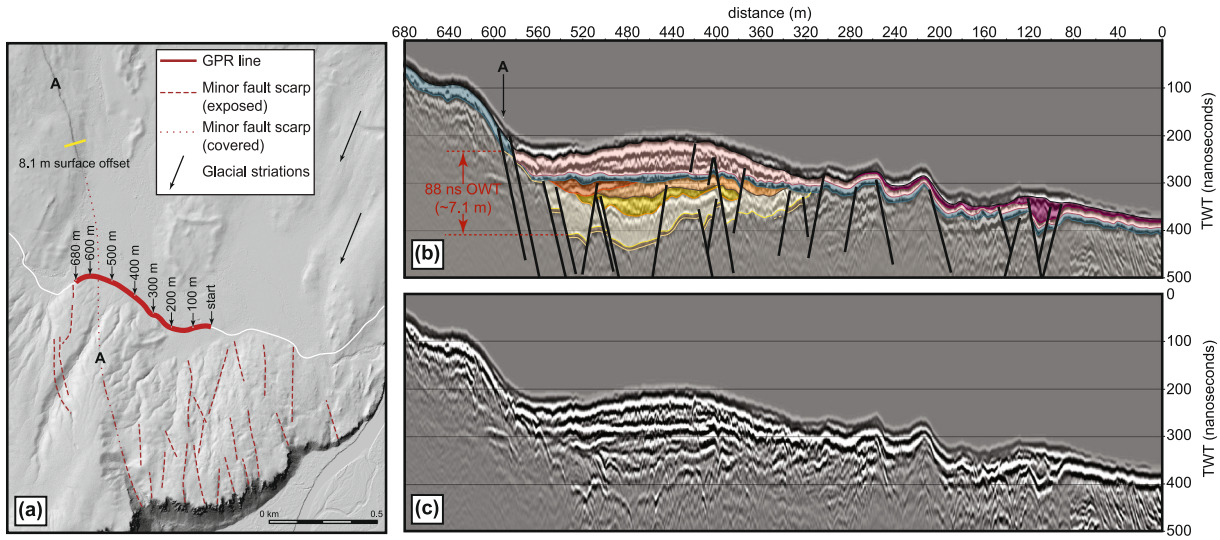

Figure 9. Ground penetrating radar (GPR) survey position and data for southern Yellowstone. (a) GPR survey line positioned to intercept interpreted zone of near-surface faulting buried by recent alluvial sediments overlying the Lewis Canyon flow. Lateral positions marked on the line correspond to *x*-axis positions on GPR line in (b) and (c). Position marked as A highlights the buried fault boundary correlated with the surface scarp to the north. Topographic profile analysis (yellow) across this scarp yields a displacement estimate of ~8 m (black text). (b) Interpreted and (c) uninterpreted GPR image, where the lateral axis is survey distance in meters, and vertical axes represent two-way travel time of the radar signal. Near surface faults were interpreted by identifying distinct sediment packages which truncate or show abrupt thinning. Displacement estimated across this feature in GPR line is ~7.1 m based upon a one-way travel time of 88 ns.

A-A′) preserve a total displacement of ~1 km across ~2.06 Ma Huckleberry Ridge flows and >4 km across the older Paleozoic-basement unconformity (Figure 4 and Table S1 in Supporting Information S1), highlighting that significant displacement on the Teton fault (>4 km) is preserved at this position and that ~75% of that displacement pre-dates eruption of Huckleberry Ridge caldera at ~2.06 Ma. Adding to this complexity, modern post-Pinedale (~14.4 ka) scarps (faults G-H on transect A-A′) recognized on the eastern shore of Jackson Lake and to the east of Steamboat Mountain (Byrd et al., 1994) yield two significant slip events that can be correlated with Teton fault events identified in trenching studies in the southern and central Tetons. This indicates that at least some seismogenic motion on the greater Teton fault system has been accommodated to the east of Steamboat Mountain (DuRoss et al., 2019, 2021; Zellman et al., 2019). This evidence of linkage between the Teton and other topographically-disconnected faults support the notion that N-S trending fault scarps across the Yellowstone caldera may link at depth.

To the south at Mount Moran (Figure 1b), a similar relationship is observed. Inverse modeling of thermochronology data indicates a maximum displacement of 11.9 ± 0.6 km over the last 9.5 ± 0.5 Ma (Thigpen et al., 2021) yet tilting of the Huckleberry Ridge tuff at the same approximate along-strike position indicates that only ~20% of that total displacement, equivalent to 2.5 ± 0.4 km (e.g., Gilbert et al., 1983, Figure S3 in Supporting Information S1), occurred over the last ~2.06 Ma. Combined, these observations suggest that: (a) significant slip (>3 km at Steamboat Mountain, >7.5 km at Mount Moran) on the Teton fault system pre-dates formation of the ~2.06 Ma Huckleberry Ridge caldera, and (b) 20%–25% of that slip accumulated on the northernmost part of the Teton fault system following the Huckleberry Ridge eruption, indicating continued motion on this fault system after caldera formation. At the along-strike position of Steamboat Mountain, a preserved total displacement of ~4 km (~1 km of which post-dates the Huckleberry Ridge) requires a minimum total fault length of ~66 km with a subsequent minimum half-length extension of 33 km to the north (Figure 1b), based on the most conservative length-displacement scaling values wherein fault displacement represents ~6% of total fault length (Curry et al., 2016; Thigpen et al., 2021).

A minimum ~33 km projection of the Teton fault north of Steamboat Mountain would significantly overlap with recently active fault scarps that offset the Lewis Canyon and Lava Creek flows in southern Yellowstone, including the Snake River caldera faults (Figure 2; Christiansen, 2001). Although the Snake River caldera faults have generally been attributed to caldera forming processes, the original mapping of Love et al. (1992) interpreted them as linked with the northern Teton fault based upon their azimuthal alignment and similar down-to-the-east motion.

Each of these features is mapped as a linear feature in aerial imagery (Figure 4c, faults D and E in Section A-A′). This interpretation has in some ways been overlooked since recognition that the seismogenic Teton fault may have recently migrated east of Steamboat Mountain (e.g., Byrd et al., 1994; DuRoss et al., 2021; Zellman et al., 2019; Figure 4c, faults G, H). However, multiple active scarps of the Snake River caldera system directly align with the interpreted position of these buried normal faults associated with the Teton system (Figure 4a), and new GPR data presented here (Figure 9) demonstrates that considerable displacement is preserved but obscured by post-Pinedale sedimentation. Accordingly, we interpret a direct kinematic linkage between the Snake River and Teton fault systems across the Huckleberry Ridge caldera boundary in the northern Tetons and southern Yellowstone.

On the northern boundary of the Huckleberry Ridge caldera, scarps accommodating recent east-west extension associated with the East Gallatin fault system also cross the caldera boundary (Figure 2). Thermochronology data for the East Gallatin fault indicate that most slip along that structure likely pre-dated formation of the Huckleberry Ridge caldera, with inverse thermal history models indicating onset of rapid cooling interpreted to represent footwall uplift at 14.4 ± 1.8 Ma. Total displacement estimates of 12.2 ± 4.1 km for the East Gallatin fault from inverse thermal history modeling yield total fault length projections of ∼203 ± 68 km, assuming displacement represents ∼6% of minimum total fault length (e.g., Curry et al., 2016; Thigpen et al., 2021). The East Gallatin fault system measures ∼40 km in total length (Koch et al., 2011; Pierce et al., 1973; USGS, 1972). Our proposed half-length extension of 102 ± 34 km south from DM is based on the thermochronologic data of Hoar (2019) and assumes that DM represents the locus of maximum displacement. If correct, this would put the southern tip of the East Gallatin fault system well into the Yellowstone caldera (Figure 10b), which is consistent with the interpretation originally proposed by Ruppel (1972).

Although the north-south trending extensional zone identified in LiDAR is partially obscured by the Pitchstone and related Central Plateau flows, it remains clearly aligned between the Teton and East Gallatin faults (Figure 2). Across this zone, total finite displacement scales proportionally with the age of the volcanic unit(s) being offset (Figures 8c and 8d), thus the lower magnitude of total extension accommodated across this zone reflects the relatively young age of the flow units. This is particularly true for the Pitchstone flow, which has an emplacement age of ∼75 ka (Stelten et al., 2015) and covers a significant part of central Yellowstone (Figure 5).

In simple models of fault growth, isolated faults are generally considered to preserve the highest magnitude of displacement near the center of the fault, with displacement decreasing to zero near the fault tips (e.g., Cowie, 1998). Larger normal fault systems are then thought to grow by the linkage of these isolated segments, commonly through direct linkage or through breached relay systems (Rotevatn et al., 2018; Figure 8e). Implicit in this model of fault growth is that for a single fault or fault sets, along-strike displacement profiles should approximately define an elliptical fault shape, and where they do not, they highlight a deviation from the rules of strain compatibility, often resulting from either truncation of part of the ellipse or transfer of displacement to another structure. At the southern tip of the Teton fault, the Hoback and Teton fault systems (Figures 1b and 10) exhibit idealized along-strike displacement distributions that would be expected between segments of a linked extensional system, with the Teton fault losing displacement to the south as the Hoback fault gains displacement (Figure 10a). However, at the current northern tip of the Teton fault and the southern tip of the East Gallatin fault, relatively high displacement values appear sharply truncated at the caldera margin (Figure 10), highlighting the potential deviation from strain compatibility mentioned above. In that scenario, the Hoback and Teton faults represent a linked system that is apparently truncated at the southern caldera margin but would have originally extended significantly farther north (>30 km), based on length-displacement scaling. Similarly, the East Gallatin fault would have originally extended considerably farther south (>100 km) based on the same length-displacement scaling relationships, but it also preserves a displacement profile indicating truncation at the northern caldera margin.

Critically, the active north-south fault scarp zone presented in this study appears to be actively evolving to link this dominantly east-west extension across the Huckleberry and Lava Creek calderas and aligns directly with the Teton and East Gallatin faults on the southern and northern caldera boundaries, respectively. Although many of the LiDAR indicated structures are relatively small, their alignment over the significant distance spanning the caldera (and dominant N-S orientation) essentially requires that they are linked via a common N-S trending master fault at depth. The existence of such a throughgoing crustal system is corroborated by the parabolic along-strike displacement profiles spanning the newly mapped fault data sets, which are interpreted as evidence that the Snake River Caldera, Mallard Lake, and cross caldera fault systems (Figure 2) have reestablished linkages across

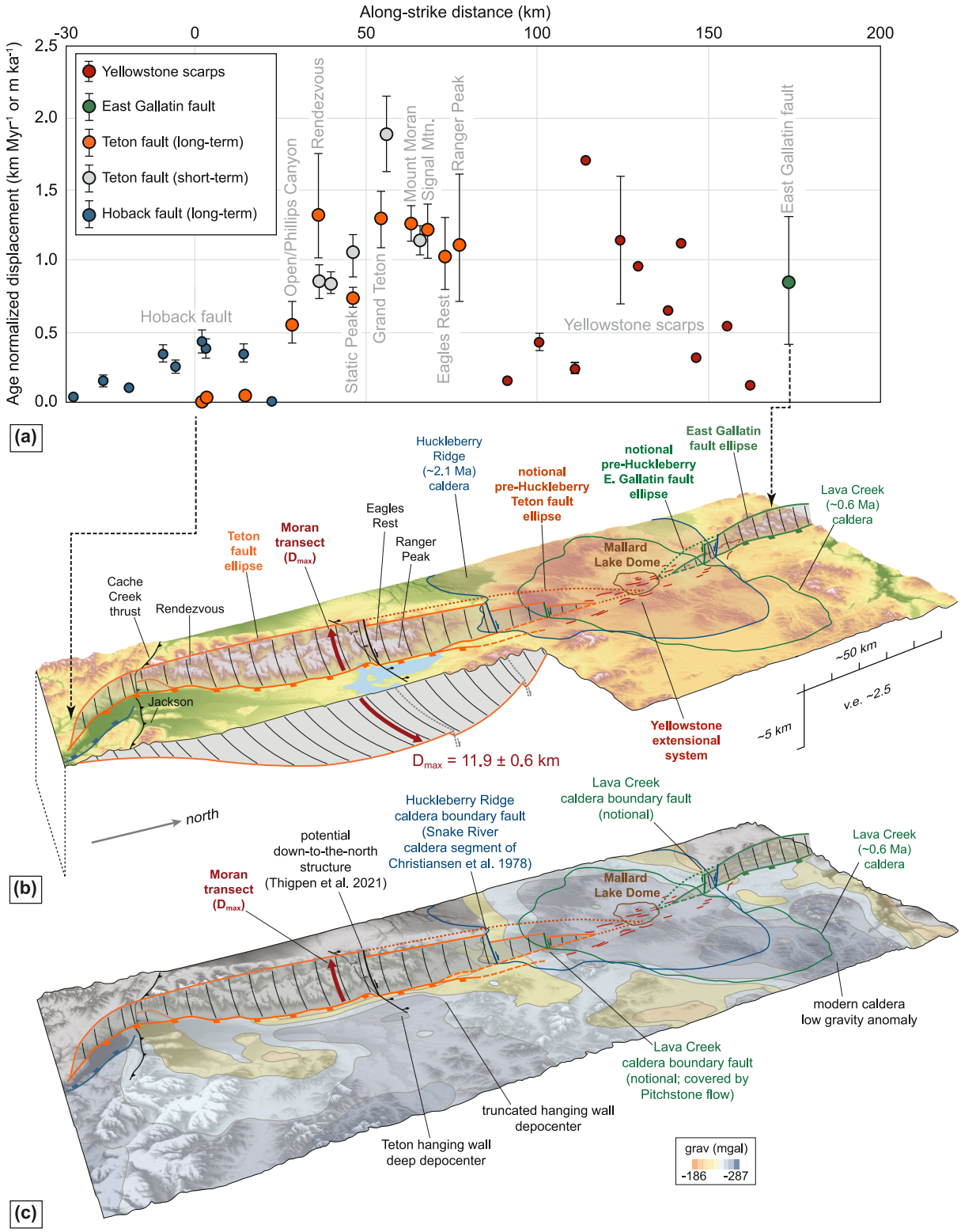
Along-strike distance (km)
-30
0
50
100
150
200
Age normalized displacement (km Myr⁻¹ or m ka⁻¹)
2.5
2.0
1.5
1.0
0.5
0.0
Yellowstone scarps
East Gallatin fault
Teton fault (long-term)
Teton fault (short-term)
Hoback fault (long-term)
Hoback fault
Open/Phillips Canyon
Rendezvous
Static Peak
Grand Teton
Mount Moran
Signal Mtn.
Eagles Rest
Ranger Peak
Yellowstone scarps
East Gallatin fault
(a)
Huckleberry Ridge (~2.1 Ma) caldera
notional pre-Huckleberry Teton fault ellipse
notional pre-Huckleberry E. Gallatin fault ellipse
East Gallatin fault ellipse
Lava Creek (~0.6 Ma) caldera
Eagles Rest
Ranger Peak
Teton fault ellipse
Moran transect (Dmax)
Mallard Lake Dome
Cache Creek thrust
Rendezvous
Jackson
~50 km
v.e. ~2.5
~5 km
Yellowstone extensional system
Dmax = 11.9 ± 0.6 km
north
(b)
Lava Creek caldera boundary fault (notional)
Huckleberry Ridge caldera boundary fault (Snake River caldera segment of Christiansen et al. 1978)
potential down-to-the-north structure (Thigpen et al. 2021)
Lava Creek (~0.6 Ma) caldera
Moran transect (Dmax)
Mallard Lake Dome
modern caldera low gravity anomaly
Lava Creek caldera boundary fault (notional; covered by Pitchstone flow)
truncated hanging wall depocenter
Teton hanging wall deep depocenter
grav (mgal)
-186
-287
(c)

Figure 10.

the caldera (Figure 8e). If the displacement magnitudes are normalized for the age of units being offset (Figure 10a), these "average" displacements exhibit a parabolic trend (except for the displacements calculated at Transect B), with higher displacements in the middle and a general decline to the north and south. Additionally, the direct scaling between the amount of displacement accommodated and the age of the flow unit being offset indicates that this deformation has persisted at least since emplacement of the oldest flow unit, the Lewis Canyon flow (853 ka; Christiansen, 2001), and is thus not fully attributable factors such as resurgent doming.

Lastly, geodetic data support the interpretation that the Yellowstone extensional zone and the Teton fault represent a linked kinematic system. Regional modeling of surface velocities from GPS stations across the interior northwestern US reveals a high strain rate zone of east-west extension that extends from the Wasatch fault in the south to the Teton Range in the north (Schmeelk et al., 2017). From central Yellowstone to the southernmost parts of Montana, extensional strain rates across this zone increase progressively with a concomitant rotation in the orientation of extension from east-west to southwest-northeast (Schmeelk et al., 2017, their Figure 6). In this modeled extensional zone, the highest modern extensional strain rates are predicted in the vicinity of the Hebgen Lake fault and are attributed to postseismic deformation following the 1959 M7.3 Hebgen Lake earthquake that resulted from rupture along a NW-SE trending normal fault (Reilinger, 1986; Savage et al., 1993). In this scenario, modern extension is limited across the East Gallatin fault, as the extension is transferred from the Yellowstone extension system to the Hebgen Lake system. However, the clearly defined pattern of recently active north-south trending fault scarps that align with the southernmost expression of the East Gallatin fault (Figure 2) indicate that this fault segment has not been completely abandoned in the modern kinematic scheme.

4.3. Absence of Footwall Topography Across Yellowstone

This growing body of data may corroborate both a paleo- and modern linkage of the Teton and East Gallatin or Hebgen Lake faults across Yellowstone. If extension has continued since at least ~853 ka, the absence of any recognizable footwall topography must also be reconciled. Essentially, if the faults were once continuous, some mechanism must be proposed to explain how the paleo-topography was removed. To the west of Yellowstone in the ESRP, the subdued topography is generally attributed to subsidence with progressive cooling of a mid-crustal mafic sill, with the lateral edges of the sill defining the abrupt relief transition that characterizes the ESRP margins (McQuarrie & Rodgers, 1998; Peng & Humphreys, 1998; Rodgers et al., 2002; Sparlin et al., 1982). Moving from southwest to northeast along the axis of the ESRP, subsidence decreases and elevation increases progressively, which is interpreted to result from time-dependent cooling and densification of mafic material in the mid-crust (McQuarrie & Rodgers, 1998; Rodgers et al., 2002). This subsidence causes the surrounding footwall ranges to show increasing amounts of crustal flexure approaching the margins of the ESRP, and when combined with subsidence produces an estimated structural relief of 4.5–8.5 km measured from the high ranges into the ESRP (McQuarrie & Rodgers, 1998). Critically, this lowering of structural relief far exceeds that which would be necessary to completely remove any footwall range topographic expression across the ESRP. However, because progressive cooling is required to produce subsidence moving away from the active mantle plume, it is difficult to imagine this mechanism driving removal of Teton and East Gallatin topography adjacent to Yellowstone.

Although the Teton Range expresses maximum relief in the vicinity of the Grand Teton, multiple studies have highlighted that the maximum displacement on the Teton fault lies east of Jackson Lake, potentially in the vicinity of Mount Moran (Brown et al., 2017; Helfrich et al., 2024; Thigpen et al., 2021). These displacement studies are corroborated by topographic analysis that indicates that the northern end of the range likely preserves greater displacement than the central Tetons, based on the amount of estimated exhumation (Zhu et al., 2021). At Mount

Figure 10. (a) Along-strike average or age-normalized displacement rate, wherein the total displacement is divided either by the age of the offset flow (Yellowstone fault scarps) or the age of fault slip onset as defined by inverse thermal history modeling of thermochronology data (Teton and East Gallatin faults). For simplicity, average displacement rates for the Hoback fault use the same onset timing of ~10 Ma as used for the Teton fault. Measured displacement, age of offset units, and calculated displacement rates are included in Table 1. (b) 3D digital elevation model (DEM) of the Teton-Yellowstone region showing the position of the Teton Range, the Yellowstone calderas, notional positions and geometries for the Teton and East Gallatin fault ellipses prior to and after the Huckleberry Ridge and Lava Creek caldera eruptions. Northern extension of the Teton fault is based on projections from length-displacement scaling of Thigpen et al. (2021). A possible down-to-the-north normal fault recognized by Thigpen et al. (2021) and the approximate positions of caldera boundary normal faults that may have accommodated "removal" of Teton and East Gallatin footwall topography are shown. (c) Same DEM surface as (b) but overlain with contoured gravity data that shows the pronounced gravity low, interpreted to represent the deepest part of the Jackson Lake basin, adjacent to Mount Moran, where the thermochronology data of Brown et al. (2017) indicated the greatest displacement on the Teton fault. The abrupt truncation of the gravity low interpreted as the Jackson Hole basin is also shown.

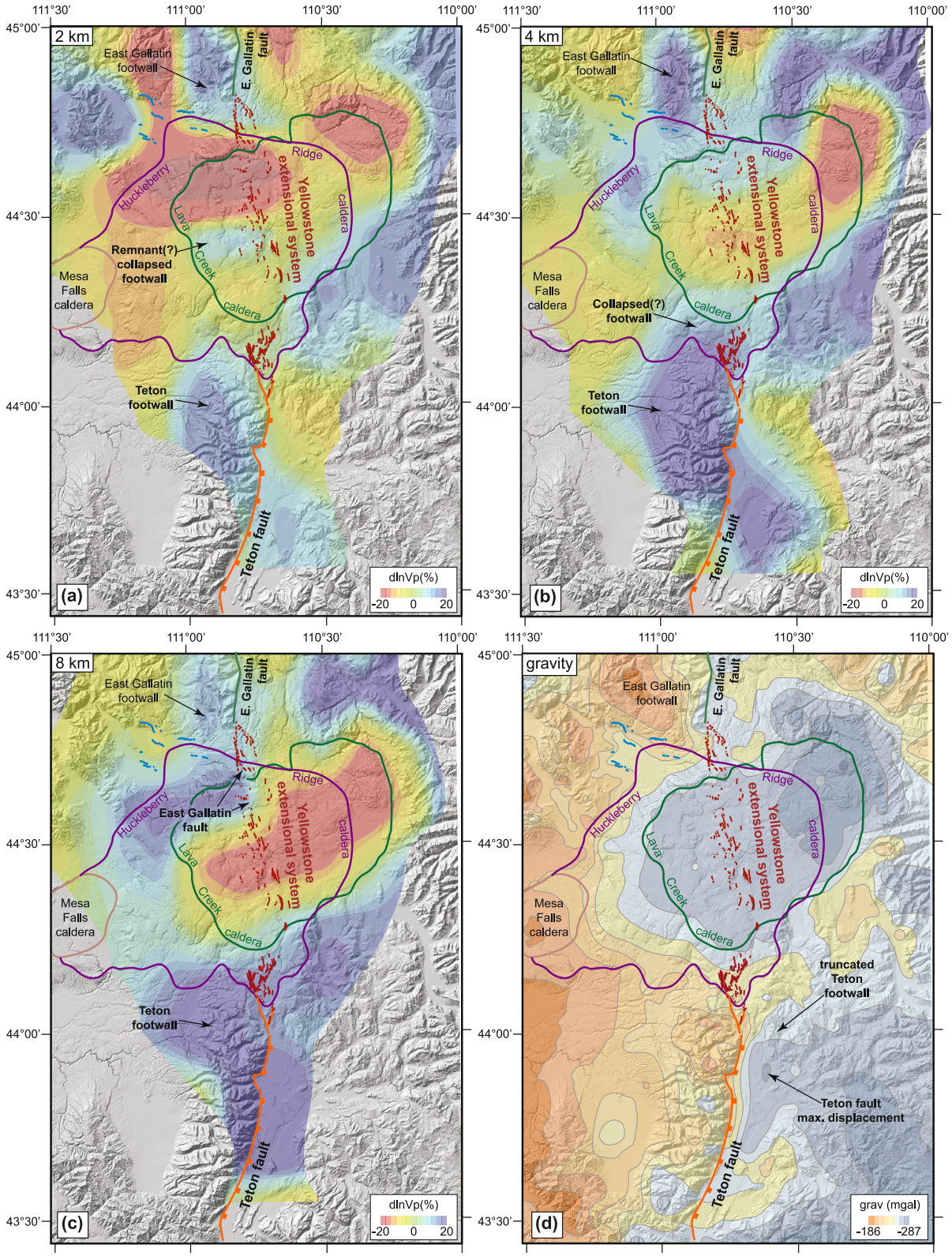
2 km
East Gallatin footwall
E. Gallatin fault
Ridge
Huckleberry
Yellowstone extensional system
caldera
Lava Creek
caldera
Remnant(?) collapsed footwall
Mesa Falls caldera
Teton footwall
Teton fault
dlnVp(%)
-20 0 20
(a)
4 km
East Gallatin footwall
E. Gallatin fault
Ridge
Huckleberry
Yellowstone extensional system
caldera
Lava Creek
caldera
Mesa Falls caldera
Collapsed(?) footwall
Teton footwall
Teton fault
dlnVp(%)
-20 0 20
(b)
8 km
East Gallatin footwall
E. Gallatin fault
Ridge
Huckleberry
East Gallatin fault
Yellowstone extensional system
caldera
Lava Creek
caldera
Mesa Falls caldera
Teton footwall
Teton fault
dlnVp(%)
-20 0 20
(c)
gravity
East Gallatin footwall
E. Gallatin fault
Ridge
Huckleberry
Yellowstone extensional system
caldera
Lava Creek
caldera
Mesa Falls caldera
truncated Teton footwall
Teton fault max. displacement
Teton fault
grav (mgal)
-186 -287
(d)
111°30'
111°00'
110°30'
110°00'
45°00'
44°30'
44°00'
43°30'

Figure 11.

Moran, total relief on the eastern range front is ∼1.8 km, however along-strike topographic swath analysis (Zhu et al., 2021, their Figure 7) indicates that Mount Moran and the Cathedral Group that includes the Grand Teton may be topographic anomalies, following similar conclusions of Foster et al. (2010). If Mount Moran and the Grand Teton are excluded, Teton Range maximum relief is on the order of ∼1.6 km. Immediately north of Mount Moran, swath topographic analysis indicates a drop in average topography of 0.5 ± 0.1 km that coincides with a considerable downward shift in relatively old apatite (U-Th)/He dates (e.g., Thigpen et al., 2021, their Figure 11). At the point where the northern Teton Range intersects the southern edge of the Huckleberry Ridge caldera, detailed mapping (e.g., Christiansen et al., 1978) combined with stratigraphic juxtaposition of units across the caldera boundary and caldera volumetric calculations (Goldsby et al., 2023) indicate a minimum ∼0.5 ± 0.1 km drop in structural relief across the caldera boundary. Alone, these two structures can account for >1.0 km of relief removal without incorporation of subsidence processes recognized in the ESRP. Although we cannot currently account for processes that would have removed the balance of our predicted remnant relief (∼0.6 km), that will be the emphasis of future studies.

The analysis above requires that the northern paleo-Teton Range (and by association the southern paleo-East Gallatin Range) may have wholly or partially collapsed into the Huckleberry Ridge or Lava Creek calderas, and analysis of geophysical data from previous studies may be consistent with this. Beneath the East Gallatin Range, upper crustal (2–8 km) depth slices through P-wave tomography models (Huang et al., 2015) may highlight the continuity of the East Gallatin fault footwall and hanging wall across both the Huckleberry Ridge and Lava Creek caldera boundaries (Figure 11). The persistence of these features at depth and their abrupt termination against the northern edge of a low *P*-wave velocity zone interpreted to reflect the upper crustal Yellowstone magmatic system indicates truncation of this structure by Quaternary development of the caldera system. On the southern boundary of the modern Yellowstone caldera, upper crustal expression of the Teton fault system is less clear in *P*-wave tomographic data, but mid-crustal depth slices (14–20 km) yield anisotropies that can potentially be correlated with the Teton system (Huang et al., 2015).

Gravity data (e.g., Carle et al., 1990; Mankinen et al., 2004) may also be consistent with the truncation of the paleo-Teton and East Gallatin Ranges by the caldera system. Immediately south of the Huckleberry Ridge caldera boundary, adjacent north-south high and low gravity anomaly trends are interpreted to represent the Teton fault footwall uplift and hanging wall basin, respectively (Figure 11d). In the Teton fault footwall, the negative anomaly widens to the north and corresponds to basin widening and deepening with increasing displacement. The negative anomaly has the widest expression along the segment of the fault with the highest estimated displacement between Mount Moran and Ranger Peaks (e.g., Brown et al., 2017; Thigpen et al., 2021). Immediately north of this zone, the negative anomaly representing the hanging wall basin terminates against the southern boundary of the Huckleberry Ridge caldera. At the position of this abrupt northern termination, the negative anomaly interpreted as the deepest and widest part of the Teton hanging wall depocenter shows little or no width tapering. Like the abrupt termination of the East Gallatin fault expressed in the *P*-wave velocity data on the northern edge of the Yellowstone caldera, this is interpreted to indicate that the northern extent of the Teton Range and its paired hanging wall basin were initially truncated and/or removed by Quaternary eruption of the Huckleberry Ridge and later caldera-forming events.

Combined, these findings are consistent with previously proposed extensions of the paleo-Teton and East Gallatin fault systems across the track of the modern Yellowstone caldera (Brown et al., 2017; Ruppel, 1972; Thigpen

Figure 11. Geophysical evidence of Teton and East Gallatin fault elements intersected and/or truncated by the Huckleberry Ridge and Lava Creek calderas. (a–c) Depth slices through the *P*-wave tomographic model of Huang et al. (2015) overlying a digital elevation model (DEM) hillshade of the Teton Yellowstone region. (a) At 2 km depth, fast *P*-wave velocity zones highlight dense crust associated with the Teton and East Gallatin Range footwall blocks. In central Yellowstone, a third zone of fast *P*-wave velocity crust that aligns with the extensional zone that links the Teton and East Gallatin faults may represent a collapsed block of paleo-fault footwall and is bound by the minor N-E and E-W trending structures mapped in Yellowstone data. (b) At 4 km depth, both footwall blocks are still preserved in the model as fast velocity zones. For the Teton footwall, the relatively high velocity crust transects the Huckleberry Ridge caldera (purple line) and is interpreted to represent the collapsed end of the paleo-Teton Range. (c) In the 8 km depth slice through the *P*-wave tomography model, the break between relatively fast footwall crust and relatively slow hanging wall crust separated by the East Gallatin fault can be seen transecting both the Huckleberry Ridge and Lava Creek caldera boundaries before being transected by relatively slow, presumably high-temperature upper crust of the modern Yellowstone caldera. (d) Bouguer gravity anomaly map draped over the DEM hillshade of the Teton-Yellowstone region. Gravity data clearly delineates the modern Yellowstone caldera boundary. The pronounced low gravity anomaly in the Teton hanging wall lies across the fault but in the same along-strike position as the maximum displacement zone identified from footwall uplift studies, which is consistent with the interpretation that the paleo-Teton fault should have extended north into Yellowstone.

et al., 2021) and critically, they provide more direct evidence of linked crustal-scale faulting north of the Teton Range. The analyses presented here also provide evidence that extension has persisted across Yellowstone since at least 853 ka as part of a larger regional east-west extension system, based on modern geodetic data (e.g., Schmeelk et al., 2017) (Figure 10b). Though LiDAR-derived estimates yield only minimum constraints of displacement across surficial structures modified by erosion and deposition, they nevertheless indicate that the newly mapped LiDAR faults must belong to a larger extensional system (Figure 10). Owing to the kinematic similarities between these faults and those of the Hoback, Teton, and East Gallatin systems, which must extend into Yellowstone to comply with empirical length-scaling relationships, we interpret that these fault systems must be kinematically linked. This interpretation requires removal of footwall topography which would have been present along this master fault system. Traditionally interpreted means of relief removal such as crustal flexure and subsidence (e.g., McQuarrie & Rodgers, 1998; Peng & Humphreys, 1998; Rodgers et al., 2002; Sparlin et al., 1982) are not likely capable of completely accounting for the absent footwall topography across the active Yellowstone system. Structural analyses indicate that collapse-related normal-sense drop of topography into the caldera or adjacent to the caldera margins can account for much of missing topography (e.g., Christiansen et al., 1978; Goldsby et al., 2023) and this structural interpretation can be corroborated by both P-wave tomography and gravity data (Carle et al., 1990; Huang et al., 2015). However, future work will need to emphasize the remainder of the missing topography (~0.6 km) across the modern Yellowstone system.

Conflict of Interest

The authors declare no conflicts of interest relevant to this study.

Availability Statement

New thermochronology data presented here is available in the System for Earth Sample Registration (SESAR; code IERPT). The Supporting Information S1 also includes a GIS shapefile for all faults mapped in this study, a separate GIS shapefile for the location of all topographic profiles used for analysis, individual figures showing the analyzed topographic profiles and accumulated displacement on fault segments, and all values calculated in the analysis.

Acknowledgments
This work was supported by NSF-EAR 1932808 to JRT, MMM, EWW, and KMY, the Overcash Field Fund at UK, a UW-NPS seed Grant to JRT and MMM, GSA Student Research Grants to RMH and MLS, an AAPG Student Grant-In-Aid to MLS, and the Kentucky Geological Survey Surface Processes and Modelling (SP&M) Laboratory.

References

Allmendinger, R. W. (1982). Sequence of late Cenozoic deformation in the Blackfoot Mountains, southeastern Idaho. In B. Bonnichsen & R. M. Breckenridge (Eds.), *Cenozoic geology of Idaho: Idaho bureau of mines and geology bulletin* (Vol. 26, pp. 505–516).

Anders, M. H., Geissman, J. W., Piety, L. A., & Sullivan, J. T. (1989). Parabolic distribution of circum-eastern Snake River Plain seismicity and latest Quaternary faulting: Migratory pattern and association with the Yellowstone hotspot. *Journal of Geophysical Research*, *94*(B2), 1589–1621. https://doi.org/10.1029/jb094ib02p01589

Anders, M. H., Spiegelman, M., Rodgers, D. W., & Hagstrum, J. T. (1993). The growth of fault-bounded tilt blocks. *Tectonics*, *12*(6), 1451–1459. https://doi.org/10.1029/93tc01547

Anderson, E. M. (1905). The dynamics of faulting. *Transactions of the Edinburgh Geological Society*, *8*(3), 387–402. https://doi.org/10.1144/transed.8.3.387

Bartel, B. (2010). UNAVCO campaign GPS/GNSS handbook: UNAVCO. Retrieved from https://kb.unavco.org/article/unavco-campaign-gps-gnss-handbook-660.html

Blackwell, D. D., & Richards, M. (2004). The 2004 geothermal map of North America explanation of resources and applications. *Geothermal Resources Council Transactions*, *28*, 317–320.

Brown, S. J., Thigpen, J. R., Spotila, J. A., Krugh, W. C., Tranel, L. M., & Orme, D. A. (2017). Onset timing and slip history of the Teton fault, Wyoming: A multidisciplinary reevaluation. *Tectonics*, *36*(11), 2669–2692. https://doi.org/10.1002/2016TC004462

Byrd, J. O. D. (1995). *Neotectonics of the Teton fault, Wyoming. Ph.D. dissertation*. University of Utah.

Byrd, J. O. D., Smith, R. B., & Geissman, J. W. (1994). The Teton Fault, Wyoming: Topographic signature, neotectonics, and mechanisms of deformation. *Journal of Geophysical Research*, *99*(B10), 20095–20122. https://doi.org/10.1029/94JB00281

Carle, S. F., Glen, J. M., Langenheim, V. E., Smith, R. B., & Oliver, H. W. (1990). Isostatic gravity map and principal facts for 694 gravity stations in Yellowstone National Park and vicinity, Wyoming, Montana, and Idaho: U.S. Geological Survey Open-File Report 90-649-B. https://doi.org/10.3133/ofr90649B

Case, J. C. (1997). Earthquakes and active faults in Wyoming. In *Geological Survey of Wyoming preliminary hazard report 97-2* (p. 58).

Christiansen, R. L. (1974). Geologic map of the west thumb quadrangle, Yellowstone National Park, Wyoming. In *U.S. Geological Survey quadrangle map GQ-1191*. https://doi.org/10.3133/gq1191

Christiansen, R. L. (2001). The Quaternary and Pliocene Yellowstone Plateau volcanic field of Wyoming, Idaho, and Montana. In *U.S. Geological Survey Professional Paper 729-G, 145, scale 1:125,000*. https://doi.org/10.3133/pp729G

Christiansen, R. L., & Blank, H. R. (1975). Geologic map of the Canyon Village quadrangle, Yellowstone National Park, Wyoming. In *U.S. Geological Survey Geologic quadrangle Map GQ-1192, scale 1:62,500*. https://doi.org/10.3133/gq1192

Christiansen, R. L., & Blank, H. R., Jr. (1974a). Geologic map of the Old Faithful quadrangle, Yellowstone, National Park, Wyoming. In *U.S. Geological Survey Geologic quadrangle Map GQ-1189, scale 1:62,500*. https://doi.org/10.3133/gq1189

Christiansen, R. L., & Blank, H. R., Jr. (1974b). Geologic map of the Madison Junction quadrangle, Yellowstone National Park, Wyoming. In *U.S. Geological Survey Geologic quadrangle Map GQ-1190, scale 1:62,500*. https://doi.org/10.3133/gq1190

Christiansen, R. L., Blank, H. R., Jr., Love, J. D., & Reed, J. C., Jr. (1978). Geologic map of the Grassy Lake Reservoir Quadrangle, Yellowstone National Park and vicinity, Wyoming. In *U.S. Geological Survey Geologic Quadrangle Map GQ-1459, scale 1:62,500*. https://doi.org/10.3133/gq1459

Cowie, P. A. (1998). A healing-reloading feedback control on the growth rate of seismogenic faults. *Journal of Structural Geology*, *20*(8), 1075–1087. https://doi.org/10.1016/S0191-8141(98)00034-0

Curry, M. A. E., Barnes, J. B., & Colgan, J. P. (2016). Testing fault growth models with low-temperature thermochronology in the northwest Basin and Range, USA. *Tectonics*, *35*(10), 2467–2492. https://doi.org/10.1002/2016TC004211

Doser, D. I. (1985). Source parameters and faulting processes of the 1959 Hebgen Lake, Montana, earthquake sequence. *Journal of Geophysical Research*, *90*(B6), 4537–4555. https://doi.org/10.1029/JB090iB06p04537

DuRoss, C. B., Gold, R. D., Briggs, R. W., Delano, J. E., Ostenaa, D. A., Zellman, M. S., et al. (2019). Preliminary paleoseismology of the Buffalo bowl trench site on the Teton fault. *Geological Society of America Bulletin*. https://doi.org/10.0410/cata/8f55cf73e40a33aa6d7cafaabfe02a24

DuRoss, C. B., Zellman, M. S., Thackray, G. D., Briggs, R. W., Gold, R. D., & Mahan, S. A. (2021). Holocene paleoseismology of the steamboat Mountain site: Evidence for full-length rupture of the Teton fault, Wyoming. *Bulletin of the Seismological Society of America*, *111*(1), 439–465. https://doi.org/10.1785/0120200212

Foster, D., Brocklehurst, S. H., & Gawthorpe, R. L. (2010). Glacial-topographic interactions in the Teton Range, Wyoming. *Journal of Geophysical Research*, *115*(F1). https://doi.org/10.1029/2008JF001135

Gansecki, C. A., Mahood, G. A., & McWilliams, M. O. (1996). $^{40}Ar^{39}Ar$ geochronology of rhyolites erupted following collapse of the Yellowstone caldera, Yellowstone Plateau volcanic field: Implications for crustal contamination. *Earth and Planetary Science Letters*, *142*(1–2), 91–107. https://doi.org/10.1016/0012-821X(96)00088-X

Gilbert, J. D., Ostenaa, D., & Wood, C. (1983). Seismotectonic study Jackson Lake Dam and Reservoir, Minidoka Project, Idaho–Wyoming. *US Bureau of Reclamation Seismotectonic Report*, *83*(3), 1–123.

Goldsby, R., Thigpen, J. R., Arimes, A., Zach, T., & Grove, R. (2023). Detailed (1:24,000) geologic mapping between Grand Teton and Yellowstone national parks: Implications for Miocene-recent extension on the Teton and related faults and the collapse of northern paleo-teton topography. *Geological Society of America Abstracts with Programs*, *55*(6), 395817. https://doi.org/10.1130/abs/2023AM-395817

Haller, K. M., Machette, M. N., & Dart, R. L. (1993). Maps of major active faults, Western Hemisphere, International Lithosphere Program (ILP), Project II-2. In *USGS open file report, 93-338*. https://doi.org/10.3133/ofr93338

Hampel, A., Hetzel, R., & Erdmann, M.-S. (2021). Postglacial slip distribution along the Teton normal fault (Wyoming, USA), derived from tectonically offset geomorphological features. *Geosphere*, *17*, 1517–1533. https://doi.org/10.1130/GES02370.1

Helfrich, A. L., Thigpen, J. R., Buford-Parks, V. M., McQuarrie, N., Brown, S. J., & Goldsby, R. C. (2024). Constraining displacement magnitude on crustal-scale extensional faults using thermochronology combined with flexural-kinematic and thermal-kinematic modeling: An example from the Teton fault: Wyoming, USA. *Tectonics*, *43*, 43–47. https://doi.org/10.1029/2024TC008308

Hoar, R. M. (2019). *Refining the onset timing and slip history along the northern part of the Teton fault. MS Thesis* (Vol. 62). University of Kentucky Earth and Environmental Sciences. Retrieved from https://uknowledge.uky.edu/ees_etds/62

Huang, H., Lin, F., Schmandt, B., Farrell, J., Smith, R., & Tsai, V. (2015). The Yellowstone magmatic system from the mantle plume to the upper crust. *Science*, *348*(6236), 773–776. https://doi.org/10.1126/science.aaa5648

Janecke, S. U., Perkins, M. E., & Smith, R. B. (2000). Normal fault pat- terns around the Yellowstone hot spot: A new model. In *Geological Society of America Abstracts with Programs, no. 7* (Vol. 32, p. A-45).

Koch, R. D., Ramsey, D. W., & Christiansen, R. L. (2011). Database for the Quaternary and Pliocene Yellowstone Plateau volcanic field of Wyoming. In *Idaho, and Montana [Digital ArcInfo rendering of maps in Professional Paper 729-G]*.

Lanphere, M. A., Champion, D. E., Christiansen, R. L., Izett, G. A., & Obradovich, J. D. (2002). Revised ages for tuffs of the Yellowstone Plateau volcanic field: Assignment of the Huckleberry Ridge Tuff to a new geomagnetic polarity event. *Geological Society of America Bulletin*, *114*(5), 559–568. https://doi.org/10.1130/0016-7606(2002)114<0559:RAFTOT>2.0.CO;2

Liccardi, J. M., & Pierce, K. L. (2008). Cosmogenic exposure-age chronologies of Pinedale and Bull Lake glaciations in greater Yellowstone and the Teton Range, USA. *Quaternary Science Reviews*, *27*(7), 814–831. https://doi.org/10.1016/j.quascirev.2007.12.005

Locke, W. W., Meyer, G. A., & Pings, J. C. (1992). Morphology of a postglacial fault scarp across the Yellowstone (Wyoming) caldera margin and its implications. *Bulletin of the Seismological Society of America*, *82*, 511–516. https://doi.org/10.1785/BSSA0820010511

Love, J. D., & Albee, H. F. (1972). Geologic map of the Jackson quadrangle, Teton County, Wyoming. In *U.S. Geological Survey miscellaneous geologic investigations map I-769-A, scale 1:24,000*. https://doi.org/10.3133/i769A

Love, J. D., & Albee, H. F. (2004). Geologic map of the Jackson quadrangle, Teton County, Wyoming. In *Wyoming State Geological Survey love map series 9, scale 1:24,000*.

Love, J. D., & Keefer, W. R. (1975). Geology of sedimentary rocks in southern Yellowstone National Park, Wyoming. In *U.S. Geological Survey professional paper 729-D, 60*. https://doi.org/10.3133/pp729D

Love, J. D., & Reed, J. C., Jr. (2000). Geologic map of the Teton Village quadrangle, Teton County, Wyoming. In *Wyoming State Geological Survey love map series 2, scale 1:24,000*. https://doi.org/10.3133/ofr75335

Love, J. D., Reed, J. C., Jr., & Christiansen, A. C. (1992). Geologic map of Grand Teton national Park, Teton County, Wyoming. In *U.S. Geological Survey miscellaneous investigations series, I2031, scale 1: 62,500*. https://doi.org/10.3133/i2031

Mankinen, E. A., Hildenbrand, T. G., Zientek, M. L., Box, S. E., Bookstrom, A. A., Carlson, M. H., et al. (2004). Guide to Geophysical Data for the Northern Rocky Mountains and adjacent areas, Idaho, Montana, Washington, Oregon, and Wyoming. In *U.S. Geological Survey open file report 2004-1413*.

McQuarrie, N., & Rodgers, D. W. (1998). Subsidence of a volcanic basin by flexure and lower crustal flow: The eastern Snake River Plain, Idaho. *Tectonics*, *17*(2), 203–220. https://doi.org/10.1029/97TC03762

Morgan, L. A., Shanks, W. C., III, Lovalvo, D. A., Johnson, S. Y., Stephenson, W. J., Pierce, K. L., et al. (2003). Exploration and discovery in Yellowstone Lake—Results from high-resolution sonar imaging, seismic reflection profiling, and submersible studies. *Journal of Volcanology and Geothermal Research*, *122*(3–4), 221–242. https://doi.org/10.1016/S0377-0273(02)00503-6

Morgan, L. A., Shanks, W. C., III, Pierce, K. L., Lovalvo, D. A., Lee, G. K., Webring, W. J., et al. (2007). The floor of Yellowstone Lake is anything but quiet—New discoveries from high-resolution sonar imaging, seismic-reflection profiling, and submersible studies. In L. A. Morgan (Ed.), *Integrated geoscience studies in the greater Yellowstone area—Volcanic, tectonic, and hydrothermal processes in the Yellowstone geoecosystem. U.S. Geological Survey Professional Paper 1717* (pp. 95–123). Retrieved from http://pubs.usgs.gov/pp/1717/downloads/pdf/Front.pdf

Nash, D. B. (1980). Morphologic dating of degraded normal fault scarps. *The Journal of Geology*, *88*(3), 353–360. https://doi.org/10.1086/628513

Nash, D. B., & Beaujon, J. S. (2006). Modeling degradation of terrace scarps in Grand Teton National Park, USA. *Geomorphology*, *75*(3–4), 400–407. https://doi.org/10.1016/j.geomorph.2005.07.027

Obradovich, J. D. (1992). Geochronology of the Late Cenozoic volcanism of Yellowstone National Park and adjoining areas, Wyoming and Idaho. In *USGS report 92-408* (pp. 1–47). https://doi.org/10.3133/ofr92408

Oglesby, D. D., & Mai, P. M. (2012). Fault geometry, rupture dynamics and ground motion from potential earthquakes on the North Anatolian fault under the Sea of Marmara. *Geophysical Journal International*, *188*(3), 1071–1087. https://doi.org/10.1111/j.1365-246X.2011.05289.x

Ostenaa, D. A., Klinger, R. E., & Levish, D. R. (1993). Holocene faulting on the Mission fault, northwest Montana. In *Geological Society of America Abstracts with Programs No. 5* (Vol. 25).

Peng, X., & Humphreys, E. D. (1998). Crustal velocity structure across the eastern Snake River Plain and the Yellowstone swell. *Journal of Geophysical Research*, *103*(B4), 7171–7186. https://doi.org/10.1029/97jb03615

Pierce, K. L. (1973). Surficial geologic map of the Mount Holmes quadrangle and parts of the Tepee Creek, Crown Butte, and Miner quadrangles, Yellowstone National Park, Wyoming and Montana. In *U.S. Geological Survey miscellaneous geologic investigations map I-640*. https://doi.org/10.3133/i640

Pierce, K. L., & Morgan, L. A. (1992). The track of the Yellowstone hotspot; volcanism, faulting and uplift. In P. K. Link, M. A. Kuntz, & L. B. Platt (Eds.), *Regional geology of Eastern Idaho and Western Wyoming* (Vol. 179, pp. 1–53). Geological Society of America Memoir.

Pierce, K. L., & Morgan, L. A. (2009). Is the track of the Yellowstone hotspot driven by a deep mantle plume?—Review of volcanism, faulting, and uplift in light of new data. *Journal of Volcanology and Geothermal Research*, *188*(1–3), 1–25. https://doi.org/10.1016/j.jvolgeores.2009.07.009

Reilinger, R. (1986). Evidence for postseismic viscoelastic relaxation following the 1959 M = 7.5 Hebgen Lake, Montana, earthquake. *Journal of Geophysical Research*, *91*(B9), 9488–9494. https://doi.org/10.1029/JB091iB09p09488

Richmond, G. M. (1973). Surficial geologic map of the Huckleberry Mountain quadrangle, Yellowstone National Park and adjoining area, Wyoming. In *U.S. Geological Survey Miscellaneous Investigation Map I-639, scale 1:62,500*.

Rodgers, D. W., Ore, H. T., Bobo, R. T., McQuarrie, N., & Zentner, N. (2002). Extension and subsidence of the eastern Snake River Plain, Idaho. In B. Bonnichsen, C. M. White, & M. McCurry (Eds.), *Tectonic and magmatic evolution of the Snake River Plain Volcanic Province* (Vol. 30, pp. 121–155). Idaho Geological Survey Bulletin.

Rotevatn, A., Jackson, C. A. L., Tvedt, A. B. M., Bell, R. E., & Blækkan, I. (2018). How do normal faults grow? *Journal of Structural Geology*, *125*, 174–178. https://doi.org/10.1016/j.jsg.2018.08.005

Ruppel, E. T. (1972). Geology of pre-tertiary rocks in the northern part of Yellowstone National Park, Wyoming. In *USGS professional paper 729-A*. https://doi.org/10.3133/pp729A

Savage, J. C., Lisowski, M., Prescott, W. H., & Pitt, A. M. (1993). Deformation from 1973 to 1987 in the epicentral area of the 1959 Hebgen Lake, Montana, earthquake (M_s = 7.5). *Journal of Geophysical Research*, *98*(B2), 2145–2153. https://doi.org/10.1029/92JB02410

Schmeelk, D., Bendick, R., Stickney, M., & Bomberger, C. (2017). Kinematic evidence for the effect of changing plate boundary conditions on the tectonics of the northern U.S. rockies. *Tectonics*, *36*(6), 1090–1102. https://doi.org/10.1002/2016TC004427

Schroeder, M. L. (1972). Geologic map of the Rendezvous Peak quadrangle, Wyoming (scale 1:24,000). In *Geologic quadrangle map GQ-980*. U. S. Geological Survey. https://doi.org/10.3133/gq980

Schroeder, M. L. (1974). Geologic map of the Camp Davis quadrangle, Teton County, Wyoming (scale 1:24,000). In *Geologic quadrangle map GQ-1160*. https://doi.org/10.3133/gq1160

Smith, E., & Bennett, K. (2006). Panther Creek volcano. *Yellowstone Science*, *14–1*, 5–12.

Smith, R. B., Byrd, J. O. D., & Susong, D. D. (1993). Seismotectonics, quaternary history, and earthquake hazards of the Teton Fault, Wyoming. *Geology of Wyoming, Memoir*, *5*, 628–667.

Sparlin, M. A., Braile, L. W., & Smith, R. B. (1982). Crustal structure of the eastern Snake River Plain determined from ray trace modeling of seismic refraction data. *Journal of Geophysical Research*, *87*(B4), 2619–2633. https://doi.org/10.1029/jb087ib04p02619

Stelten, M. E., Cooper, K. M., Vazquez, J. A., Calvert, A. T., & Glessner, J. J. G. (2015). Mechanisms and timescales of generating eruptible rhyolitic magmas at Yellowstone caldera from Zircon.

Telbisz, T., Gabor, K., Szekely, B., & Szabo, J. (2013). Topographic swath profile analysis: A generalization and sensitivity evaluation of a digital terrain analysis tool. *Zeitschrift für Geomorphologie*, *57*(4), 485–513. https://doi.org/10.1127/0372-8854/2013/0110

Thigpen, J. R., Brown, S. J., Helfrich, A. L., Hoar, R. M., McGlue, M. M., Woolery, E. W., et al. (2021). Removal of the Northern Paleo-Teton range along the Yellowstone hotspot track. *Lithosphere*, *2021*, 1–27. https://doi.org/10.2113/2021/1052819

United States Geological Survey. (2016). *GrandTetonElkRefuge 2014, United States Geological Survey 3D elevation Program*. Distributed by OpenTopography. Retrieved from https://portal.opentopography.org/usgsDataset?dsid=USGS_LPC_WY_GrandTetonElkRefuge_2014_LAS_2016

United States Geological Survey. (2021). *YellowstoneNP 2 2020, United States Geological Survey 3D Elevation Program*. Distributed by OpenTopography. Retrieved from https://portal.opentopography.org/usgsDataset?dsid=WY_YellowstoneNP_2_2020

United States Geological Survey Water Resources Division. (1972). Geologic map of Yellowstone National Park. In *USGS Numbered Series 771*. https://doi.org/10.3133/i711

Wilson, C. W. (1934). Geology of the thrust fault near Gardiner, Montana. *The Journal of Geology*, *42*(6), 649–663. https://doi.org/10.1086/624221

Witkind, I. J. (1964). Reactivated faults north of Hebgen Lake. In *The Hebgen Lake, Montana, earthquake of August 17, 1959. U.S. Geological Survey Professional Paper 435-G* (pp. 37–50). https://doi.org/10.3133/pp435

Witkind, I. J. (1975). Preliminary map showing known and suspected active faults in Idaho. In *U.S. Geological Survey open file report, 75-278*. https://doi.org/10.3133/ofr75278

Wotzlaw, J. F., Ilya, N. B., Stern, R., D'Abzac, F., & Schaltegger, U. (2015). Rapid heterogeneous assembly of multiple magma reservoirs prior to Yellowstone supereruptions. *Nature Scientific Reports*, 5–14026. https://doi.org/10.1038/srep14026

Zellman, M. S., DuRoss, C. B., & Thackray, G. D. (2019). The Teton Fault, Wyoming Geological Survey open file report, Teton county, Wyoming.

Zhu, Y., Dortch, J. M., Massey, M. A., Haneberg, W. C., & Curl, D. (2021). An intelligent swath tool to characterize complex topographic features: Theory and application in the Teton Range, Licking River, and Olympus Mons. *Geomorphology*, *387*, 107778. https://doi.org/10.1016/j.geomorph.2021.107778

References From the Supporting Information

Dortch, J. M., Tomkins, M. D., Saha, S., Murari, M. K., Schoenbohm, L. M., & Curl, D. (2022). A tool for the ages: The probabilistic cosmogenic age analysis tool (P-CAAT). *Quaternary Geochronology*, *71*, 101323. https://doi.org/10.1016/j.quageo.2022.101323

Flowers, R. M., Ketchum, R. A., Shuster, D. L., & Farley, K. A. (2009). Apatite (U–Th)/He thermochronometry using a radiation damage accumulation and annealing model. *Geochimica et Cosmochimica Acta*, *73–8*, 2347–2365. https://doi.org/10.1016/j.gca.2009.01.015

Gallagher, K. (2012). Transdimensional inverse thermal history modeling for quantitative thermochronology. *Journal of Geophysical Research*, *117*(B2), 373. https://doi.org/10.1029/2011JB008825

Morgan, L. A., & McIntosh, W. C. (2005). Timing and development of the Heise volcanic field, Snake River Plain, Idaho, western USA. *Geological Society of America Bulletin*, *17*(3), 288–306. https://doi.org/10.1130/B25519.1